DEPARTMENT OF PHYSICS
UNIVERSITY OF JYVÄSKYLÄ
RESEARCH REPORT No. 3/2013

MODELING THE ATOMIC AND ELECTRONIC STRUCTURE OF NANOPARTICLE-LIGAND INTERFACES.

BY

VILLE MÄKINEN

Academic Dissertation
for the Degree of
Doctor of Philosophy

To be presented, by permission of the Faculty of Mathematics and Natural Sciences of the University of Jyväskylä, for public examination in Auditorium FYS1 of the University of Jyväskylä on March 22th, 2013 at 12 o'clock noon

UNIVERSITY OF JYVÄSKYLÄ
Jyväskylä, Finland
February 2013

Preface

This work has been done at Nanoscience Center (NSC) of the University of Jyväskylä during 2009-2012.

I would like to thank Professor Hannu Häkkinen for focusing my attention to nanosciences already when I was a student, subsequently offering me a possibility to do my master's degree in his group, and finally offering me a postgraduate position in his computational nanoscience group. I thank Dr. Pekka Koskinen for introducing me to the tight-binding method and for the possibility to participate in the implementation in the form of the `hotbit` code. I also thank Dr. Karoliina Honkala for the opportunity to work in the field of surface science. I thank all the above mentioned for discussion and guidance during this time. I would like to thank Professor Matti Alatalo and Professor Adam Foster for reviewing my thesis and for helpful comments.

This work has been funded by the Academy of Finland FINNANO program and by the Department of Physics. The main part of the computations were done at CSC – the Finnish IT Center for Science in Espoo.

A great thanks goes to the staff of the NSC and the Department of Physics, especially for the administration personnel. Working here has been enjoyable. I thank Dr. Pekka Koskinen and Prof. Ilari Maasilta for the possibility to participate in teaching by having me as an exercise assistant on their physics courses. I thank all my friends at JYU, especially the Holvi collaboration, for the lunch break discussions, related and not-related to physics. I thank my parents and my brother, and especially my girlfriend Agata, for support and also giving me something other to think than physics.

Jyväskylä, February 2013
Ville Mäkinen

Abstract

Thiolate-protected gold clusters have been studied intensively since their first synthetization two decades ago. We studied the thermodynamical properties of one of the well-known cluster, $Au_{25}(SR)^{-}_{18}$, via density functional theory molecular dynamics simulations. Based on our 10 ps simulations in temperatures between 300 K and 600 K the weakest bonds in the cluster are in the core-thiolate interface. However, we did not observe bond breakings, which suggests that the cluster is extremely stable, in agreement with previous experimental observations. The superatom electronic structure, which is previously seen only in ground state calculations, is now identified in the presence of thermal vibrations.

We applied the density-functional tight-binding method to study the same cluster by developing the parametrizations for the important chemical interactions in the model cluster $Au_{25}(SH)^{-}_{18}$. We were able to show that tight-binding can reproduce both the atomic and electronic structure to satisfactory accuracy. The symmetry of the atomic structure was preserved and the superatom structure was seen in the electronic states. However, more benchmarking is required before the tight-binding can be reliably used in novel studies.

Aluminum oxide growth in the atomic layer deposition process over the titanium dioxide nanoparticles, present in dye-sensitized solar cells, was studied using density functional theory. We found out that the aluminum oxide layer is not uniform after the first deposition cycle but contains holes. This indicated that the electrolyte present in the solar cell may still be able to contact the titanium dioxide, thus decreasing the power conversion efficiency. Also the binding of dye molecules is affected, lifting the standard N3 dye molecule ~ 1.7 Å higher, weakening the electronic coupling between the molecule and the titanium dioxide. It is therefore questionable whether the aluminum oxide layer can help to improve the efficiency of the cells.

Author's address Ville Mäkinen
Department of Physics
University of Jyväskylä
Finland

Supervisor Professor Hannu Häkkinen
Department of Physics and Department of Chemistry
University of Jyväskylä
Finland

Co-supervisors Docent Karoliina Honkala
Department of Chemistry
University of Jyväskylä
Finland

Academy Fellow Researcher Pekka Koskinen
Department of Physics
University of Jyväskylä
Finland

Reviewers Professor Matti Alatalo
Department of Mathematics and Physics
Lappeenranta University of Technology
Finland

Professor Adam Foster
Department of Applied Physics
Aalto University School of Science
Finland

Opponent Dr. Gemma Larsen
Department of Chemistry
University of Copenhagen
Denmark

List of publications

This thesis is based on the following four publications:

I P. Koskinen and V. Mäkinen. *Density-functional tight-binding for beginners.* Computational Materials Science **47**, 237 (2009).

II V. Mäkinen, P. Koskinen and H. Häkkinen. *Modeling thiolate-protected gold clusters with density-functional tight-binding.* The European Physical Journal D *in press.*

III V. Mäkinen and H. Häkkinen. *Density functional theory molecular dynamics study of the* $Au_{25}(SR)^-_{18}$ *cluster.* The European Physical Journal D **66**, 310 (2012).

IV V. Mäkinen, K. Honkala and H. Häkkinen. *Atomic Layer Deposition of Aluminum Oxide on* TiO_2 *and Its Impact on N3 Dye Adsorption from First Principles.* The Journal of Physical Chemistry C **115**, 9250 (2011).

The author has performed all of the calculations in articles II and III, and most of the calculations in article IV. The author has written the drafts of articles II, III and IV. The author has helped to develop the `hotbit` program introduced in article I, and has calculated tests and examples for the article I. In addition, the author has carried out some calculations for the following articles, and participated in writing some parts for the articles.

V C. L. Heinecke, T. W. Ni, S. Malola, V. Mäkinen, O. A. Wong, H. Häkkinen and C. J. Ackerson. *Structural and Theoretical Basis for Ligand Exchange on Thiolate Monolayer Protected Gold Nanoclusters.* The Journal of the American Chemical Society **134**, 13316 (2012).

VI L. J. Antila, M. J. Heikkilä, V. Mäkinen, N. Humalamäki, M. Laitinen, V. Linko, P. Jalkanen, J. Toppari, V. Aumanen, M. Kemell, P. Myllyperkiö, K. Honkala, H. Häkkinen, M. Leskelä and J. E. I. Korppi-Tommola. *ALD Grown Aluminum Oxide Submonolayers in Dye-Sensitized Solar Cells: The Effect on Interfacial Electron Transfer and Performance.* The Journal of Physical Chemistry C **115**, 16720 (2011).

VII E. B. Guidez, V. Mäkinen, H. Häkkinen and C. M. Aikens. *Effects of Silver Doping on the Geometric and Electronic Structure and Optical Absorption Spectra of the* $Au_{25-n}Ag_n(SH)^-_{18}$ *(n=1, 2, 4, 6, 8, 10, 12) Bimetallic Nanoclusters.* The Journal of Physical Chemistry C **116**, 20617 (2012).

Contents

1 Introduction

1.1 The structure of matter

The understanding of what matter is has been evolving along mankind. For example, in ancient Greece the constituents of all matter were four elements: fire, earth, air and water. Sometimes aether was added to the list as the fifth element.[1] In the absence of accurate measuring devices and proper experiments, this kind of model of the world worked well enough, as there was no experimental evidence that would falsify the theory. For example, let's imagine that we have a gold bar and we cut it in half. The two halves do not differ from the original bar other than in size and weight, so in this experiment the gold behaves as continuous, homogeneous material.

Over the centuries people invented more sophisticated measuring devices and conducted different experiments. It started to become evident that the five-element model was not adequate enough. The discovery of an electron by Thomson[2] first led to a model, where the negatively charged particles are confined in a positive homogeneous matter (the plum pudding model). Then Rutherford presented experimental results that the positive charge must be also gathered into small blocks, and the atom nucleus was discovered.[3]

After that we have learned that these subatomic particles behave in a way that cannot be explained by classical physics, and quantum physics was developed, starting from Planck's work on black body radiation in 1900. We know that nuclei consist of both protons and neutrons, which again consist of even smaller particles, called quarks. We have found many other particles that are not stable and do not exist free in nature, but can be seen (indirectly) e.g. in large hadron collider (LHC) at CERN. At the time of writing this thesis, two groups working at LHC announced that they have found another particle, which may turn out to be the Higgs boson of the standard model.[4, 5]

Here I will make a rough categorization of physics, using the above-mentioned gold bar as a demonstration tool. The region where we are splitting macroscopic gold bars in two can be described as classical physics. In the other end where we are splitting individual gold atoms goes into the area of nuclear physics. When splitting the protons and neutrons of the nucleus we are talking about high energy physics, or particle physics. Between the classical and nuclear physics there is a region, where the gold particles become so small that their properties begin to differ from the bulk properties. These phenomena begin to emerge when the particles are in the nanometer (10^{-9} m) scale (i.e. nanoparticles), and therefore this field is called nanoscience.

The emerging phenomena are connected partly to the surface-area-to-volume (sa/vol) ratio which grows as the particle size gets smaller. In another words, more

and more atoms are located at the surface of the particle as opposed to being in the bulk environment. This has interesting consequences. In bulk phase the atoms often form a crystal structure, because it minimizes the free energy. With high sa/vol ratio, it might be more advantageous to minimize the surface energy instead, and the atomic configuration becomes different than the bulk crystal structure.

The change in the structure affects many other properties, for example how the cluster absorbs light. Bulk gold is yellowish, but gold nanoparticles appear to be red (this was noticed already in the Middle Ages; the red colour in glass paintings was often achieved by grinding gold into powder and mixing it into the glass. The reason was, however, not understood). Another good example is that even though the bulk gold is highly inert material (it does not react easily with other compounds), the gold nanoparticles, especially on a proper substrate, are highly reactive and work as a catalyst for many reactions.[6] Suggested explanations include for example charge effects and a high number of low coordinated atoms.[7, 8]

It is then obvious that our knowledge about bulk materials cannot be blindly applied to nanoparticles of the same material. One aim of nanoscience is to develop general understanding of how the different properties of materials change as the size of the particles is reduced. Then it is possible to make predictions of what kinds of materials one should study in order to achieve some desired properties.

The gold bar was just a simple example, but similar things are happening e.g. in the semiconductor industry. The basic building block of virtually all the modern electronic devices, the transistor, has been already squeezed into so tiny volume that further minimizing is forbidden by the quantum-mechanical phenomena that cause uncontrollable electrical leakage in the system. Therefore it is necessary to develop completely new types of electronic components, and for example it has been shown that it is possible to reliably hold one bit of information using only 12 Fe atoms.[9]

1.2 Thiolate-protected gold clusters

As mentioned briefly before, bare gold nanoparticles are highly reactive, which makes it difficult to control them and study them experimentally in detail. They can be produced in vacuum, and some properties, like electron diffraction, can be subsequently measured.[10] However, when they are deposited on substrate, their shape tends to change, they are often quite mobile and coalesce with each other to form larger clusters.[11] All this makes it difficult to not only study them but also use them in applications.

There are many envisioned applications for the small gold particles.[12] One of the most interesting is to use them in cancer treatment.[13] The gold atoms, being heavy elements, absorb radiation more efficiently than organic material. If we could attach the gold clusters to tumors, a larger portion of the irradiation

would concentrate into the tumor, thus reducing the collateral damage to the neighbouring healthy tissue. Another possibility is to use them as markers. The gold nanoparticle doped tumors could be seen clearer in X-ray images or with some other imaging methods, e.g. with UV[14] or Raman[15] spectroscopy. On some surfaces they drain charge from the substrate and can act as a catalyst.[16]

The bare reactive clusters are impossible to deal with but they can be passivated by a layer that isolates the cluster and inhibits it from reacting with other molecules. Already three decades ago Briant et al. managed to produce small gold clusters that were surrounded by phosphine ligands[17], and in 1994 Brust et al. managed to synthesize similar clusters with thiolate[1] (SR) ligands.[18] After the first synthetization the study of monolayer(ML)[2] protected clusters has been intense. It was found that clusters with specific masses were substantially more stable than others, but there was no rigorous explanation for that.

The big breakthrough was made in 2007 when Jadzinsky et al. were able to crystallize one of these clusters, $Au_{102}(SR)_{44}$, and resolve its atomic structure precisely.[19] This is shown in figure 1 (although with smaller ligands for clarity). Subsequently the electronic structure was calculated with state-of-the-art computational methods[20], and a better understanding of thiolate-protected gold clusters was achieved.

The stability can be explained by two factors. First, the atomic configuration is highly symmetric. The center of the cluster is pure gold arranged in five-fold D_{5h} symmetry. It is protected by RS−Au−SR and RS−Au−S(R)−Au−SR units that are also arranged in symmetric fashion on the gold core surface. Second, the electronic structure resembles that of a noble gas atom. The arguments explaining the stability and non-reactivity of the noble gas atoms can be generalized to these clusters to some extent, and therefore atomic clusters showing this type of behaviour are named superatoms.

So far the atomic structure of three different thiolate-protected clusters has been resolved. These are $Au_{25}(SR)_{18}$ in both anionic[21, 22] and neutral[23] form, $Au_{38}(SR)_{24}$[24] and $Au_{102}(SR)_{44}$.[19] The search for new stable clusters is ongoing and the mass and composition of many relatively stable clusters are known.[25–28] For the $Au_{144}(SR)_{60}$ there is already a promising theoretical prediction for the atomic structure.[29]

In the cancer treatment applications, it is not enough that the clusters are protected. They should also selectively attach to cancer cells. This could be achieved by replacing or modifying the ligands in the protecting layer by molecules that are designed to attach to specific environments. The partial, selective ligand-

[1]Thiol is a molecule with a general structure R−S−H, where R is a carbon-containing group, and thiolate is a thiol from where the H is removed.

[2]Monolayer is a layer that consists of molecules of only one type, completely covers the surface, and is only one molecule thick.

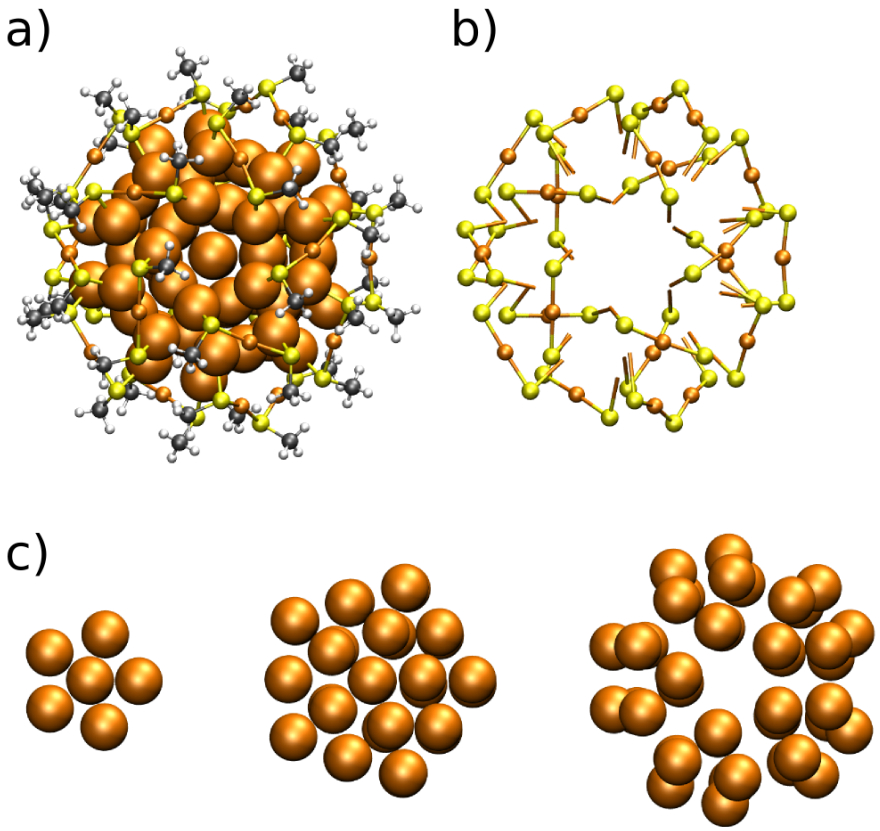

Figure 1: The structure of the $Au_{102}(SR)_{44}$, the first thiolate protected cluster whose atomic structure was resolved. The real ligands are replaced by methyl groups for clarity. a) The full atomic structure. b) The protecting layer composed of S−Au−S and S−Au−S−Au−S units. c) The three concentric shells of the metallic gold core.

exchange has been performed with $Au_{102}(SR)_{44}$, which is an important step in learning to design the ligand layer for different purposes.[30]

More research on the thiolate-protected gold clusters is needed in order to realize their envisioned applications. The next section deals with dye-sensitized solar cells, which are already operational, and more work is needed mainly to make them commercially more viable.

1.3 Dye-sensitized solar cells

Worldwide energy consumption is increasing constantly.[31] At the same time the price of oil is increasing as the old oil deposits are drying up and new ones are

harder to exploit. The traditional energy production methods (oil, coal, natural gas) release greenhouse gases into the atmosphere, and the climate is warming at alerting rate.[32] Therefore renewable energy has become worthy option and different ways to harness renewable energy sources are studied and developed.

One of the most popular and straightforward ways is to convert sunlight directly into electricity. This can be done with solar cells. They are manufactured from semiconducting material, and the sunlight is used to excite electrons from the valence band to the conduction band of the semiconductor. The formed electron-hole pairs subsequently separate and create electric current.

In traditional solar cells the semiconductor of choice is silicon. In silicon the band gap is about 1.0 eV, which is narrow enough for visible light to excite electrons from valence to conduction band. The main reason for the high price of traditional solar cells is the expensive process of purifying silicon.

In 1991 O'Regan and Grätzel developed a new, cheaper way to produce solar cells.[33–35] They replaced the silicon with considerably cheaper titanium dioxide. Unfortunately, the band gap of TiO_2 is three times wider compared to the silicon, so visible light is not energetic enough to excite electrons. To overcome this problem the titanium dioxide is covered with dye molecules to sensitize it to visible light. These cells are therefore called dye-sensitized solar cells (DSSC).

The principles of the operation of a DSSC is shown in figure 2. The visible light excites an electron of a dye molecule from the highest occupied molecular orbital (HOMO) to the lowest unoccupied molecular orbital (LUMO) (arrow 1). Subsequently the excited electron tunnels from the dye into the conduction band of the TiO_2 (arrow 2). Some energy is wasted as the electron relaxes to the bottom of the conduction band (arrow 3). The injected electron travels through the TiO_2 layer to the anode and to the external circuit (arrow 4). The circuit is closed when the dye acquires a missing electron from the electrolyte (arrow 5).

The cell efficiency is highly dependent on the ability of the dye molecule to capture photons and inject the excited electrons into the titanium dioxide. Several sensitizer molecules have been developed and tested. Currently the standard molecule is called N3 (proper formula is $Ru(dcbpy)_2(NCS)_2$, where dcbpy = 4,4'-dicarboxy-2,2'-bipyridine), which is shown in figure 3. After it's introduction more efficient molecules have been discovered recently, for example CYC-B19.[36]

Currently the top efficiency of the DSSCs ($\sim 10\,\%$) is far behind the values of the silicon solar cells ($\sim 40\,\%$)[37] (these are record values, the commercial cells are naturally less efficient). There are many processes that decrease the conversion efficiency of the DSSCs. The electron that is already injected into the TiO_2 may recombine directly with the electrolyte at the surface of the TiO_2 (arrow 6) or with a dye molecule that is missing an electron (arrow 7). Both of these events take place at the TiO_2 surface. Inside the TiO_2 the traveling electron might get trapped

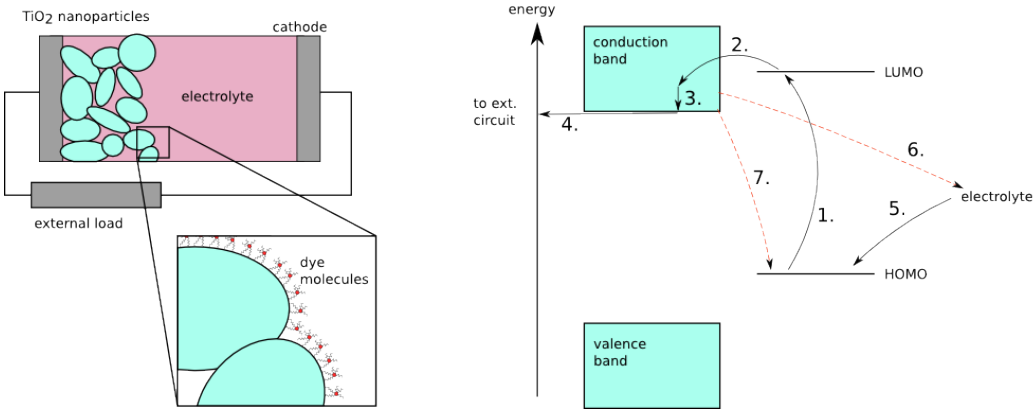

Figure 2: Left: The schematic structure of the dye-sensitized solar cell. The anode is coated with TiO_2 nanocrystals that are sintered together. Then they are covered with dye molecules. The circuit is closed by electrolyte which connects the TiO_2-dye combination to the cathode. Right: The energy schematics of the operation of DSSC.

into the potential wells created by the defects in the crystal.

The electron injection rate depends on how the molecule interacts with the titanium dioxide, which in turn is determined by orientation the molecule is adsorbed on the surface. The adsorption geometry has been studied for example by analyzing the shifts in IR spectrum, and also computer simulations have been employed.[38–41] The optimal adsorption on the clean anatase (101) surface is via one COOH groups from both dcbpy-groups.

Some studies indicated that the efficiency could be increased by coating the titanium dioxide with a thin layer of another oxide before attaching the dyes.[42] The idea is to create a barrier which prevents the electrolyte molecules from coming too close to the surface and the electrons tunneling back from the TiO_2. This naturally also slows down the tunneling from the dye molecule to the titanium dioxide, but this reaction is so fast that it is not the limiting factor and can thus be slowed down to some extent.[43]

There are many methods to coat materials, e.g. chemical vapor deposition (CVD) and sol-gel process, just to name a few.[44, 45] Perhaps the most accurate method (in terms of surface thickness) to grow thin films is the atomic layer deposition (ALD) method.[46, 47] With ALD various materials can be grown on the surface of many substrates. It is a sequential process, and the steps are described in figure 4. In the first step the substrate is exposed to a precursor molecule A. In an ideal case the A molecules adsorb on the substrate but not on top of each other, so after the first step the substrate is completely covered with A molecules. In the

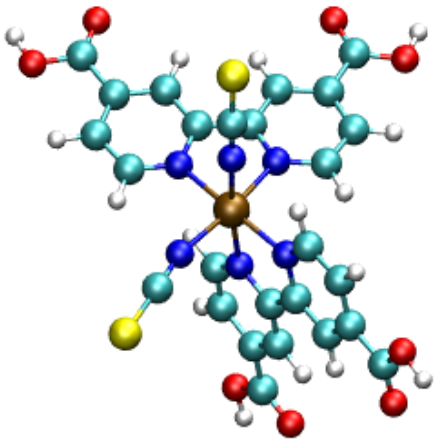

Figure 3: The standard dye molecule N3. In the center there is a ruthenium atom (brown). To it is connected two NCS groups and two planar organic groups. The COOH groups (four) are used to attach the molecule to the surfaces. Colors: Brown-Ru, dark blue-N, light-blue-C, yellow-S, red-O, white-H.

second step the surface is exposed to precursor molecules B which react with A molecules, but not with each other. Ideally after the second step the substrate is covered with a layer of AB molecules. This is called the first ALD cycle, and by repeating the cycle one can grow many layers of new material and of course control the thickness of the layer to high accuracy.

In reality the process is not that perfect. The molecules are not like LEGO® blocks that perfectly match each other, the molecules can be adsorbed to different orientations etc. Also the precursor molecules may be so big that steric repulsion prevents a formation of a full monolayer in a single ALD cycle. As a result there will be holes left on the layers and the forming surface will not be perfectly smooth. Also the lattice constants of different materials are not the same, so there will probably be some sort of amorphous region at the interface which connects the original and new crystal structures.

While ALD is often used to coat the substrate with another compound, it is also possible to grow the same material. The task for every substrate-coating combination is to find suitable precursor molecules. Ref. [47] lists many tested combinations, and it can be seen that the ALD is a highly versatile process.

Because the ALD does not work ideally, the structure of the coating (especially at the substrate-coating interface) is not known. Therefore the process has been studied computationally to get a deeper understanding of the structure of the interfaces and the formation processes.[48–57]

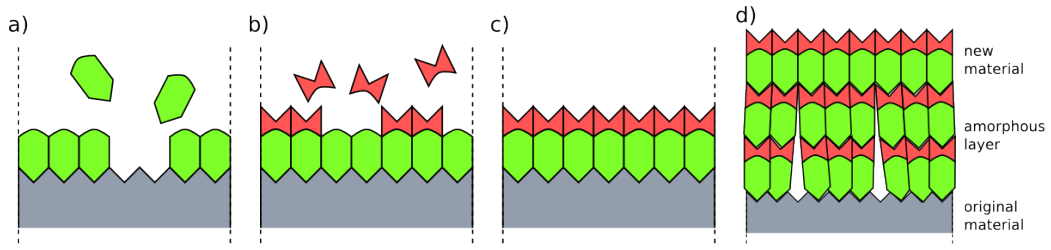

Figure 4: The ideal ALD process. a) The original surface (grey) is exposed to precursor A (the green particles). They adsorb on the surface but not onto each other. b) The treated surface is then exposed to precursor B (red particles) that again only adsorb onto A particles. c) The surface after one ALD cycle. d) More realistic picture of the layer formation.

1.4 Computational modeling of atomic systems

The dimensions of nanoscale systems are comparable to the atomic distances. This means that usually individual atoms must be simulated explicitly to have a realistic model of the system. In addition, calculating the electronic structure is often vital to have reliable results and to understand the properties of the systems.

I have used two different simulations methods in my work. One method is called the density functional theory (DFT). It is in widespread use and is a well tested method, and there is good understanding of to what kind of studies it fits and which properties are reliably reproduced. The DFT is popular method because it provides good accuracy with reasonable computational costs. The importance of the method is emphasized by the fact that Walter Kohn was awarded the Nobel prize in 1998 for the development of the DFT. I used the method to study both the thiolate-protected gold clusters and titanium dioxide surfaces.

The problem with DFT (as with all the methods) is that the computational demands grow as a function of the system size. Density-functional tight-binding (DFTB) is an approximation to the DFT that tries to capture the essential parts but at the same time reduce the complexity of the problem. The DFTB calculations require orders of magnitude less computational resources, but this comes with the cost of decrease in the accuracy and transferability. I studied the possibility to use DFTB to study the thiolate-protected gold clusters.

Simulation methods require some sort of information about the systems we are simulating. It can include macroscopic properties of the material (e.g. density or electric conductivity), or in the case of atomistic simulation, information about the atoms in the system. Depending on the level of theory, element-specific information can be enough. In more approximative approaches also the interactions between the elements may be included into the parameters. One part of my work was to

develop these kinds of parameters (mainly for the gold and sulfur) to be able to simulate thiolate-protected gold clusters using DFTB.

2 Theoretical research methods

2.1 The principles of theoretical modeling

Modeling reality with theoretical models and computers is challenging. Even though computational power has been growing exponentially, often we cannot run many interesting simulations due to insufficient resources. This means that we must simplify our theoretical models. Therefore the models we use in simulations do not always reflect our best knowledge of the real physical world, but are approximations that capture the most essential parts.

The simplest approximation to do atomistic simulations is to treat the atoms as classical balls. The interaction between the atoms can be modeled e.g. with Lennard-Jones pair-potential

$$V(r) = 4\varepsilon \left(\left(\frac{\sigma}{r}\right)^{12} - \left(\frac{\sigma}{r}\right)^{6} \right), \tag{1}$$

where r is the distance between the atoms and the parameters ε and σ are fitted to e.g. experimental results. The first term approximates the Pauli repulsion and the second long-range van der Waals attraction[3].

This approach works adequately for noble gas atoms, which do not interact chemically with each other. It is too simple to model different kinds of bondings between the atoms (e.g. covalent versus metallic), and more parameters must be added to the model if one wants to simulate chemical reactions.[58] However, in reality the chemical bonds are the manifestation of the electron gas relaxing to the lowest energy configuration. Therefore simulating reactions with classical potentials requires tuning several parameters, and some properties (for example the optical absorbance) are simply out of reach because the method does not contain information about the electronic structure.

The accuracy and reliability of the simulations can be increased by taking the electronic structure into account explicitly. The electrons are such small particles that the laws of classical physics cannot be blindly applied to describe them. Instead they are described with quantum mechanics, which explains many phenomena that classical physics cannot (for example why the electrons orbiting the atoms do not radiate energy away and collide with the nucleus).

The standard way to do electronic structure calculations is to invoke the Born-Oppenheimer approximation. It states that because the atomic nuclei are ≥ 2000 times heavier than electrons, their movement can be decoupled. In practice this means that we can always assume that the electrons have had time to relax to the

[3]The form of the first term is simply an approximation for the repulsion, and the exponent was chosen to be 12 so that it is faster to calculate it as the square of the second term.

movement of the nuclei, and they are always in the lowest energy configuration. Moreover, again because the nuclei are heavier, we treat them as classical balls, and the electrons we treat with quantum mechanics.

With this model e.g. the hydrogen atom can be solved even analytically, and the results agree perfectly with the experimental absorption spectra. However, the hydrogen atom is the simplest possible example one can imagine. In my work with clusters and surfaces there are tens or even hundreds of atoms, and there are no more analytic solutions available. We must resort to treat the problems numerically.

2.2 Quantum mechanics for calculating the electronic structure

It is evident that we need information about the electronic structure of the systems we are studying to get accurate results. The electrons are small particles that cannot be described with Newtonian mechanics; we need to dive into quantum mechanics.

In quantum mechanics the total energy of the system is represented by the Hamiltonian operator $\hat{H}$. For electrons in any system it can be written as

$$\hat{H} = \hat{T} + \hat{V}_{\text{ext}} + \hat{W}, \tag{2}$$

where the first term represents the kinetic energy of the electrons, the second is the potential energy of the electrons in the external potential (caused by the atom nuclei and e.g. external electric field) and the last is the Coulomb energy of the electrons. Here we have ignored e.g. relativistic corrections and spin-orbit couplings. For light elements this is justified[59], but for heavy nuclei (e.g. gold) it is necessary to include relativistic corrections.[60]

The electrons are not described by classical particles at specific position, but by an abstract state $|\Psi\rangle$. When the Hamiltonian operates on the state, it returns the total energy of the system

$$\hat{H}\,|\Psi\rangle = E\,|\Psi\rangle \ . \tag{3}$$

These are abstract concepts, and in practice we must often choose some representation to do actual calculations. Perhaps the easiest to grasp is the real-space representation, where we project the state into real-space:

$$\langle \vec{r}\,|\Psi\rangle = \Psi(\vec{x}_1, \vec{x}_2, ..., \vec{x}_N), \tag{4}$$

where $\vec{x}_i = (\vec{r}_i, \chi_i)$ is the position and the spin of the electron. The projection is called the wave function. The square norm of the wave function, $|\Psi(\vec{x}_1, \vec{x}_2, ..., \vec{x}_N)|^2$,

is proportional to finding one electron at point $\vec{r}_1$ with spin χ_1, another at $\vec{r}_2$ with spin χ_2 and so on. In real-space representation the Hamiltonian (in unit system where $\hbar = m = e = 1$) takes the form

$$\hat{H} = \sum_i^N -\frac{1}{2}\nabla_i^2 + \sum_i^N v_{\text{ext}}(\vec{r}_i) + \sum_i^N \sum_{j>i}^N \frac{1}{|\vec{r}_i - \vec{r}_j|}, \tag{5}$$

where v_{ext} is the external potential created by the nuclei. In the case of hydrogen atom, the eigenvalue equation in the real-space reduces into

$$-\frac{1}{2}\nabla_1^2\Psi(\vec{r}_1) + v_{\text{ext}}(\vec{r}_1)\Psi(\vec{r}_1) = E\Psi(\vec{r}_1), \tag{6}$$

which can be solved analytically because the electron-electron interaction term vanishes and the external potential is simple enough (spherically symmetric).

Usually the analytic solving of the problem is impossible, and we must resort to numerical methods. But even then we immediately run into problems. Let's say we want to simulate the two electrons of the hydrogen molecule H_2 in a simulation box of $10\,\text{Å} \times 10\,\text{Å} \times 10\,\text{Å}$ with grid spacing $0.2\,\text{Å}$. This gives us `grid points` $\times$ `spin` $= \left(\frac{10\,\text{Å}}{0.2\,\text{Å}}\right)^3 \times 2 = 250\,000$ values for each coordinate $\vec{x}_i$. For N particles the $\Psi(\vec{x}_1, \vec{x}_2, ..., \vec{x}_N)$ is then an object with $(250\,000)^N$ values. If the value of the wave function at each point is saved as double precision complex number (which uses 16 bytes (B) of memory), then the memory required to express the whole many-body wave function of the H_2 is roughly

$$(250\,000)^2 \times 16\,\text{B} = 1\,000\,000\,000\,000\,\text{B} \sim 930\,\text{GB} \tag{7}$$

It is obvious that this kind of direct approach takes us nowhere. Fortunately, there are ways to go around this problem.

2.3 Density functional theory

The exponential dependence (on the number of electrons) of the computational demands can be avoided by the use of density functional theory (DFT). It is mainly based on two important pieces of work that enable us to simplify calculations considerably: the Hohenberg-Kohn theorem[61] and the Kohn-Sham approach[62] for its implementation.

The Hohenberg-Kohn theorem (in its simplest form only valid for non-degenerate ground states) shows that there is one-to-one mapping (bijection) between the potentials and the electron densities. Here two potentials are considered different if they differ more than by a constant. It follows that the ground state wave function

and ground state observables are functionals of the electron gas density. Especially the ground state total energy can be written as

$$\begin{aligned} E\left[n\right] &= \langle\Psi[n]|\,\hat{V}_{\text{ext}} + \hat{T} + \hat{W}\,|\Psi[n]\rangle = V_{\text{ext}}[n] + T[n] + W[n] \\ &= \int_1 v_{\text{ext}}(\vec{r}_1)n(\vec{r}_1) + F[n] \\ &= \int_1 v_{\text{ext}}(\vec{r}_1)n(\vec{r}_1) + E_{\text{H}}[n] + G[n], \end{aligned} \tag{8}$$

where $\int_1 := \int d\vec{r}_1$ and $E_{\text{H}}[n]$ is the classical Coulombic energy, called Hartree energy

$$E_{\text{H}}[n] = \frac{1}{2}\int_1\int_2 \frac{n(\vec{r}_1)n(\vec{r}_2)}{|\vec{r}_1 - \vec{r}_2|}, \tag{9}$$

v_{ext} is again the external potential, and F and G are universal functionals of the electron gas density $n(\vec{r})$. Since there is one-to-one mapping between the electron density and potentials, only one density gives the ground state and therefore the variation of the total energy at the ground state density vanishes:

$$\frac{\delta}{\delta n(\vec{r})}E[n] = 0 \quad \Rightarrow \quad \frac{\delta}{\delta n(\vec{r})}G[n] = -v_{\text{ext}}(\vec{r}) - v_{\text{H}}(\vec{r}), \tag{10}$$

where we defined the Hartree potential

$$v_{\text{H}}(\vec{r}) = \int_2 \frac{n(\vec{r}_2)}{|\vec{r}_2 - \vec{r}|}\ . \tag{11}$$

This is huge simplification, since in principle it allows us to find the ground state of the system by varying the electron gas density, which is much simpler object than the many-body wave function. It is real-valued and positive, and the formalism is the same regardless of the number of electrons (as opposed to the wave function in equation (4) which gets more and more complex as the number of electrons is increased). The problem is that the Hohenberg-Kohn theorem does not provide any means to actually calculate the total energy. In equation (8) the largest constituent of the functional G is the kinetic energy of the electrons, and we don't know how to calculate that from the electron gas density.

To get forward we use the approach developed by Kohn and Sham.[62] In the derivation of the Hohenberg-Kohn theorem the interaction between the particles is not relevant, so it is applicable even if the particles do not interact at all. In the Kohn-Sham (KS) approach we switch from the original system to auxiliary system of non-interacting electrons. From the HK theorem we know that such a potential v_{s} exists that produces the same electron density as in the interacting case. We can then write the Hamiltonian as

$$\hat{H}_{\text{s}} = \hat{T} + \hat{V}_{\text{s}}[n]. \tag{12}$$

From now on I will concentrate strictly on fermionic systems, i.e. systems, that contain only spin-$\frac{1}{2}$ particles. Since there is no interaction between the auxiliary electrons, the many-body wave function (of the auxiliary electrons) Ψ_s can be expressed as a Slater determinant of orthogonal single particle states ψ_i:

$$\Psi_\mathrm{s}(\vec{x}_1, \vec{x}_2, ..., \vec{x}_N) = \frac{1}{\sqrt{N!}} \sum_{\sigma \in S_N} \mathrm{sgn}(\sigma) \prod_{i=1}^{N} \psi_i(\vec{x}_{\sigma_i}), \tag{13}$$

where the S_N is the set of permutations of length N. For simplicity I will only consider systems that are spin-paired, i.e. each state has electron with spin up and spin down (it is possible to do spin-polarized calculations, we just need separate spin-up and spin-down densities).

In spin-paired cases we can split the eigenvalue equation

$$\hat{H}_\mathrm{s} \left|\Psi_\mathrm{s}\right\rangle = E_\mathrm{s} \left|\Psi_\mathrm{s}\right\rangle \tag{14}$$

into N/2 single particle equations

$$\Big\{ -\frac{1}{2}\nabla^2 + v_\mathrm{s}(\vec{r}) \Big\} \psi_i(\vec{r}) = \varepsilon_i \psi_i(\vec{r}) \quad \text{for} \quad i = 1, ..., N/2. \tag{15}$$

We need N/2 states because only two electrons (with spin up and spin down) can be put in the same state. The electron density and total energy are obtained from

$$n(\vec{r}) = 2 \sum_{i=1}^{N/2} \left|\psi_i(\vec{r})\right|^2, \tag{16}$$

$$E_\mathrm{s} = 2 \sum_{i=1}^{N/2} \varepsilon_i = T_\mathrm{s} + \int_1 v_\mathrm{s}(\vec{r}_1) n(\vec{r}_1), \quad \text{with} \tag{17}$$

$$T_\mathrm{s} = 2 \sum_{i=1}^{N/2} \left\langle \psi_i \right| -\frac{1}{2}\nabla^2 \left|\psi_i\right\rangle \ . \tag{18}$$

The ε_i is the energy of the single particle state ψ_i and T_s is the kinetic energy of the non-interacting system (see the section 2.4.2).

The main idea of the Kohn-Sham approach is to use the kinetic energy of the non-interacting system as an approximation for the kinetic energy of the real physical system, so therefore we define

$$G[n] = T_\mathrm{s}[n] + E_\mathrm{XC}[n], \tag{19}$$

where the term $E_\mathrm{XC}[n]$ is called the exchange-correlation (XC) energy. By definition it contains the energy due to the purely quantum-mechanical interactions and the

difference between the real and non-interacting kinetic energies. In the final form the total energy of the real physical system is written as

$$E[n] = \int_1 v_{\text{ext}}(\vec{r}_1)n(\vec{r}_1) + \frac{1}{2}\int_1\int_2 \frac{n(\vec{r}_1)n(\vec{r}_2)}{|\vec{r}_2 - \vec{r}_1|} + T_{\text{s}}[n] + E_{\text{XC}}[n]. \tag{20}$$

At the ground state density the variation vanishes, i.e.

$$\frac{\delta}{\delta n(\vec{r})}E[n] = 0 = v_{\text{ext}} + v_{\text{H}} + \frac{\delta}{\delta n(\vec{r})}T_{\text{s}} + v_{\text{XC}}, \tag{21}$$

where we defined

$$v_{\text{XC}}[n](\vec{r}) = \frac{\delta}{\delta n(\vec{r})}E_{\text{XC}}[n]\ . \tag{22}$$

It can be shown that $\frac{\delta}{\delta n(\vec{r})}T_{\text{s}} = -v_{\text{s}}$, so we get

$$v_{\text{s}} = v_{\text{ext}} + v_{\text{H}} + v_{\text{XC}}\ . \tag{23}$$

As the v_{s} is used in calculating the single particle states and energies using equation (15), the exchange-correlation functional affects the calculations in much deeper way than simply by affecting the total energy in equation (20).

The Kohn-Sham approach does not provide a direct solution to the many-body problem, but an iterative scheme where the set of equations are solved self-consistently until the solutions converge. The algorithm to solve the equations is in principle:

1. Create an initial guess for the single-particle wave functions (can be random, but more physical initial guess speeds up the calculation).

2. Calculate the electron density from the wave functions using equation (16).

3. Calculate the Hartree and exchange-correlation potentials from the electron density using (11) and (22).

4. Solve the single-particle equations (15) using the previously-calculated potentials to get new wave functions and the total energy.

5. If the total energy and/or the wave functions changed more than some convergence criteria, go back to step 2. Otherwise, the problem is considered solved.

The Kohn-Sham method is iterative, i.e. we have to repeat the solving cycle several times to get a solution that is converged well enough.

2.3.1 The exchange-correlation functional

We introduced the exchange-correlation functional when we approximated the real kinetic energy with the non-interacting kinetic energy. The XC functional therefore contains the difference between these two energies. In addition it contains all the purely quantum-mechanical effects we have not included so far. This is problematic term in DFT since we don't know how the XC functional should look like. Many different approximations have been developed using numerous arguments. I will not go into details on how to approximate the term but only give two common examples.

In **local density approximation** (LDA) we think that the electron gas is divided into small cubes where the gas density is constant, and calculate the E_{XC} as the sum over these cubes. The mathematical way to say this is that we integrate the XC energy density of the uniform electron gas $\epsilon_{\mathrm{XC}}^{\mathrm{unif.}}$ multiplied by the electron density:

$$E_{\mathrm{XC}}^{\mathrm{LDA}}[n] = \int_1 \epsilon_{\mathrm{XC}}^{\mathrm{unif.}}(n(\vec{r}_1))n(\vec{r}_1), \tag{24}$$

where the uniform electron gas energy density $\epsilon_{\mathrm{XC}}^{\mathrm{unif.}}$ is taken from Monte Carlo simulations. This gives surprisingly good results for various different systems, but it is obvious that it does not take into account the density gradients.

The next step in approximating the E_{XC} is to include the density gradients into the functional. The exchange-correlation functionals of this type are called **generalized gradient expansion** (GGA) functionals. In general the GGAs are of the form

$$E_{\mathrm{XC}}^{\mathrm{GGA}}[n] = \int_1 f(n, \nabla n)(\vec{r}_1) \ . \tag{25}$$

They are called semi-local functionals, because even though they use information around the point of evaluation, they do not contain any long-range effects. Following the reasoning, it is possible to include also higher order derivatives of the density into the functionals, but they have not achieved as high same popularity.

There are numerous different functionals developed with different approaches. Some are derived purely from the theoretical basis while others contain parameters that are fitted to some (experimental) data (these are called semi-empirical functionals). An open source collection of exchange-correlation functionals `libxc` lists tens of different LDA parametrizations, GGAs and higher-order functionals.[63] In my work I have been using Perdew-Burke-Ernzerhof (PBE) GGA functional.[64] It is derived strictly from theoretical basis and it performs well on a variety of systems. The semi-empirical functionals often perform better with small molecules (and they are often used in chemistry) but in solid state physics LDA and PBE usually perform better.

2.4 Implementation of the density functional theory

2.4.1 Simulation cell and boundary conditions

In DFT we are modeling a small region of space. This is called the simulation cell. The cell is defined by three lattice vectors, which are often chosen to be orthogonal (but don't have to be). The atoms are then inserted inside the cell, where they can move during the simulation.

The boundary conditions define how the particles see the simulation cell walls. There are basically two types of boundary conditions. **Free boundary conditions** mean that the particles cannot escape the cell; there the cell walls act like infinite potential barriers. This is natural if we are simulating e.g. molecules or clusters in gas phase. In DFT the wave functions must vanish at the boundaries, so the cell walls cause non-physical forces to the atoms that are too close to the walls. Therefore it is necessary to ensure that there is always several Ångströms of empty space between the atoms and the walls.

The boundary conditions can also be **periodic**, which means that the simulation cell is repeated infinitely to every direction. If the particle crosses the simulation cell wall, it can be transferred to the opposite side of the cell. Periodic boundary conditions are used when simulating e.g. bulk materials. It should be noted that this is highly simplistic picture. In reality the crystals always contain lattice defects and impurities. If the material consist mainly of single crystal structure and the impurities and defects do not play crucial role, this approach can give reasonable results.

We have used open-source python package called Atomic Simulation Environment (ASE) to manage the atoms in simulations.[65] In ASE it is possible to apply the periodic boundary conditions to some directions and let the rest have free boundary conditions. This is especially convenient for simulating elongated structures (periodic in one direction) and surfaces using slab models (periodic in two directions).

From periodic boundary conditions it follows that the external potential (that the electrons experience) has translational symmetry. When solving the single particle equations in such a potential we end up to the Bloch's theorem, which states that the solutions are so-called Bloch wave functions. They do not vanish at the edges anymore but get a phase shift proportional to the wave vector of the wave function.[66]

There are materials that do not have any crystal structure, i.e. they are amorphous. The way to simulate those kinds of materials is to choose periodic boundary conditions, and in addition choose a simulation cell large enough so that the periodicity is effectively screened.

2.4.2 Electronic temperature and state occupations

Usually when switching to non-interacting system we need more than N/2 single-particle states, for both physical and technical reasons.

When the single-particle equations are solved, it is possible that the HOMO is degenerate. In those cases there is no physical reason to favor any of those states, i.e. we don't know where to assign the last electrons. In addition, the degenerate states are not spherically symmetric, so assigning electrons to only some of them would result into non-spherical ground state, which is unphysical if the external potential is spherical (mainly in the case of isolated atoms). For example the isolated Boron atom has electronic structure [He].$2s^2.2p^1$, and assigning the last electron to any $2p$ state would result to non-spherical atom. Similar problem arises with metals, which have high density of states at the Fermi level.

This problem is solved by giving each state an occupation number, which does not have to be an integer. In practise we modify the equation (16) - (18) by replacing the multipliers 2 with occupation numbers $f_i \in [0, 2]$ and adding more states into the calculation:

$$n(\vec{r}) = \sum_{i=1} f_i \left|\psi_i(\vec{r})\right|^2, \tag{26}$$

$$E_\mathrm{s} = \sum_{i=1} f_i \varepsilon_i = T_\mathrm{s} + \int_1 v_\mathrm{s}(\vec{r}_1) n(\vec{r}_1), \quad \text{and} \tag{27}$$

$$T_\mathrm{s} = \sum_{i=1} f_i \left\langle \psi_i \right| -\frac{1}{2}\nabla^2 \left|\psi_i\right\rangle \ . \tag{28}$$

The electrons are fermions so they follow Fermi-Dirac statistics. The occupation numbers are therefore obtained from the Fermi-Dirac distribution

$$f_i = \frac{2}{\exp[(\varepsilon_i - E_\mathrm{F})/k_\mathrm{B}T] + 1}, \tag{29}$$

where E_F is the Fermi energy and $k_\mathrm{B}T$ is usually set from 0 eV to 0.1 eV. This has the effect that near the Fermi level little population is transferred from the occupied states to the unoccupied ones, and it mimics the thermal excitations of the electrons. This procedure is necessary whenever the density of states is high at the Fermi energy (as is often with metals). It also gives degenerate states equal occupations.

There are also technical reasons for the empty states in the calculations. One of the mostly used algorithms to solve the single-particle equations is called RMM-DIIS (residual minimization scheme, direct inversion in the iterative subspace[67]). With this algorithm converging the highest single-particle states included in the calculation is difficult. Therefore it is necessary to have some empty states in the calculation so that the occupied state can be converged efficiently.

2.4.3 Basis functions

Because we are working with computers and numerical computations, the wave functions must be represented somehow on the computer. This is achieved by choosing a suitable set of functions (basis set), and expanding the wave functions as a linear combinations of these functions. There are basically three different types of basis sets: real-space grid[4], plane-waves and localized atomic orbitals. I will briefly explain these in more detail.

Real-space grid is perhaps the most straightforward way to express the wave functions. The simulation cell is divided into uniform boxes, and each box contains the (average) value of the wave function in that box. The finer the grid spacing h is the more accurately the wave functions can be expressed. However, simultaneously the memory requirements grow as $\left(\frac{1}{h}\right)^3$ and the calculations become slower. The trick is to find the optimum grid density so that the results do not change (notably) if it is further raised.

The wave functions can also be expressed as a linear combinations of **plane waves,** i.e. linear combinations of functions $\{e^{i\vec{k}\cdot\vec{r}}\}$. Since the plane waves form a complete set, an infinite expansion would give infinite accuracy, but again in practice we must terminate the expansion at some point. The energy of the plane wave is related to the wave vector as $E \sim |\vec{k}|^2$, and the expansion is terminated when the energy exceeds a predefined value, called cut-off energy. As with the grid basis, one must find the optimum cut-off energy to find good balance between the accuracy and the computational demands.

Although from the mathematical point of view the grid and plane wave basis are the same thing expressed in different way (one can Fourier-transform from one to another), in practice they behave differently, and both have useful properties and weaknesses. For example, in real-space grid integrals are easy to divide into separate spatial regions and parallelize over several cores. In plane wave basis getting the value of the wave function at a specific coordinate requires evaluating the value of each basis function multiplied with the coefficient. In plane wave basis increasing the accuracy of the calculation can be easily done by increasing the cut-off value. Mathematically this means simply adding more functions to the basis set, and usually the computed values converge smoothly. With grid, increasing the grid spacing changes all the previous grid points, and the positions of the atoms w.r.t. the grid points change. Often this leads to the oscillation of the total energy (and other values), and can sometimes cause problems.

With the grid and plane waves each part of the simulation cell is treated with equal precision. This is not the case with **the localized basis** sets. The basis functions are centered at the atomic nuclei, and the functions are (often) calculated

[4]One can argue that grid is not a basis set, but from technical point of view there is no reason to treat it differently.

from single atom calculation, so they resemble atomic orbitals. They are designed to represent electron wave functions near the atoms, but the inter-atomic region cannot be reproduced as accurately as with previous two basis sets. It is therefore challenging to describe highly non-local electrons with localized basis set. The advantage is that for systems, where this kind of basis is good enough, the use of localized basis functions is often orders of magnitude faster.

With grid and plane wave basis the basis set is chosen before the calculation. This is different with localized basis set, where each atom contains some number of basis functions. This means that the more there are atoms in the simulation cell, the better the basis set is. From this fact arises a serious problem, called basis set superposition error. It can be explained by simple example of calculating the adsorption energy of a molecule on the surface. First we calculate the total energies of the clean surface and the molecule in gas phase. Then we calculate the total energy of the system, where the molecule is adsorbed on the surface. However, now both the molecule and the surface have more basis functions available than in the previous calculation. This means that the total energies are not strictly comparable, and the adsorption energy (calculated as the difference of the separated systems and the adsorbed system) may contain considerable errors. This error can be decreased by adding so-called ghost atoms on the clean surface and gas phase molecule calculations. It means that we don't add real atoms in the system, but the same basis function (at the same places) as in the combined system, so that the isolated systems can benefit from the same extra basis functions.

2.4.4 Projector-augmented wave method and core states

The parts of the wave functions between the atoms are considerably smoother compared to the parts close to the atomic nuclei, where they often oscillate rapidly. Whether using a grid or plane waves as a basis, representing these oscillations accurately would require so dense grid or so large plane wave basis that it is practically impossible. The way to circumvent this problem is to treat the spatial region near the nuclei separately.

One way to do this is to use projector-augmented waves (PAW). In this approach there are regions around the nuclei (augmentation spheres) where the wave functions are represented using pre-calculated partial wave functions. They are element-specific, and represent well the oscillations of the wave functions near the nuclei. They are generated by performing a DFT calculation for an isolated atom with dense grid. For heavy elements the relativistic effects are taken into account by scalar-relativistic approximation.

In PAW calculations most operations are performed with smooth pseudo wave functions, but whenever needed, there is a linear transformation that augments the pseudo wave functions with the partial waves and returns the normalized

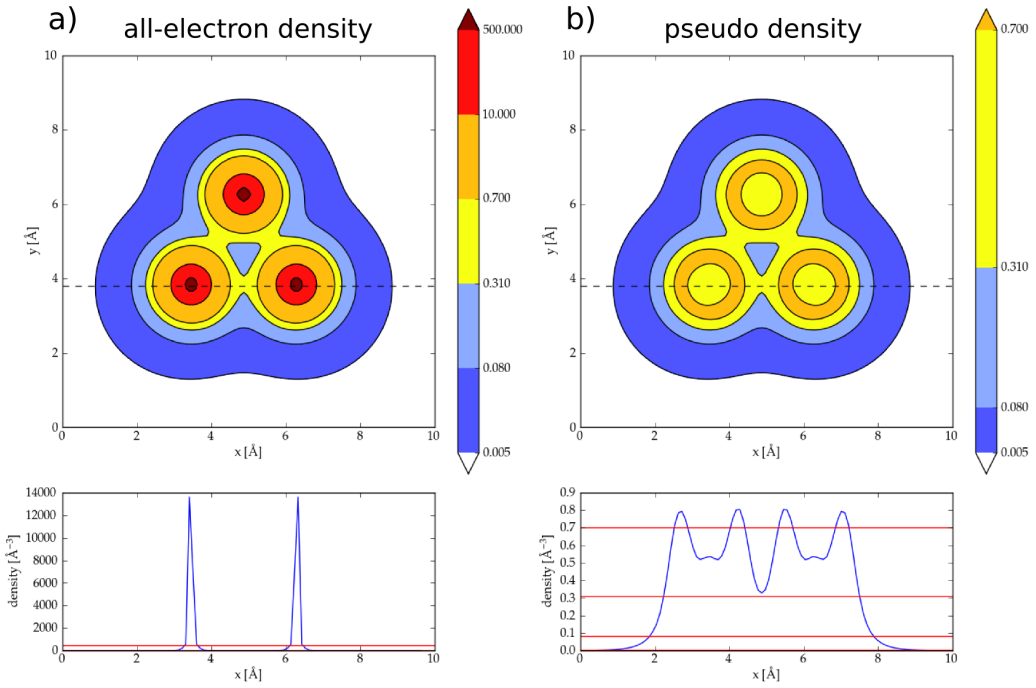

Figure 5: The all-electron and pseudo densities of the Au_3^- cluster in the plane $z = 0\,\text{Å}$, calculated with the GPAW DFT code. Upper figures show the cross sections of the densities at $z = 0\,\text{Å}$. The all-electron density is localized near the atom nuclei, but the pseudo density has maximum values around the nuclei at the augmentation sphere edges. Lower figures show the densities along the line $z = 0\,\text{Å}, y = 3.8\,\text{Å}$ (marked in the upper figures). Note that the color bar in panel a is not linear.

all-electron wave function. The advantage is that the smooth pseudo wave function can be stored in coarse grid and only inside the augmentation spheres the grid is denser. In figure 5 the all-electron and pseudo density of Au_3^- are shown.

We are often interested in studying systems with several hundreds of atoms. Simulating a bare gold cluster with 100 atoms (each contains 79 electrons) would mean solving the KS equations for roughly 4000 electronic states[5]. If the simulation cell is a cube with side length 20 Å, the grid spacing 0.2 Å, the wave functions can

[5]Assuming spin-paired calculation (two electrons per state) and some empty states

be chosen to be real-valued, we would need

$$\frac{(20\,\text{Å})^3}{(0.2\,\text{Å}^3)} \times 4000 \times 8\,\text{B} = 32\,000\,000\,000\,\text{B} = 29.8\,\text{GB}$$

memory for simply to store all the wave functions of a spin-paired calculation. This specific example could be calculated, but it shows that calculations quickly become very demanding.

Often in solid-state physics and in chemistry we are interested in atomic structures and chemical bonding. These are both mainly determined by the valence electrons of the atoms. The core electrons sit considerably closer to the atomic nuclei and do not participate in bond formation. This is the reason why elements in the same columns of the periodic table have similar chemical properties: their valence electron shells are similar. Therefore to make calculations less demanding it is common strategy to explicitly simulate only the valence electrons, and treat the core electrons as frozen. In the previous example this would reduce the number of needed states from 4000 to 600. This means that we do not have KS single electron wave function for each electron. The total density is however obtainable by augmenting the pseudo-density with the core electron contributions.

2.4.5 Limitations of the DFT

In the derivation of DFT we have used several mathematical tricks, the most obvious being switching into non-interacting system and single-particle equations. However, they are all mathematically rigorous and, as implied by the HK theorem, the electronic density in the equations corresponds to the *real* electronic density.

The only part where we really have to do an approximation is when we give an explicit form for the exchange-correlation functional. As explained in the chapter 2.3.1 there are many options to choose from. Because of this term even the electron density contains some errors, and their shape and magnitude depends on which XC functionals we are using.

As can be seen from equation (15) the exchange-correlation functional directly affects the KS states. Unfortunately there is no unique way to rank the functional according to their performance. For example the LDA, the simplest XC functional, gives better bulk gold lattice constant than the more sophisticated PBE. Often the rationale for choosing the XC functional for the calculations is to choose the one that gives best results e.g. in terms of the lattice constant or band gap width when compared to experimental values. However, one quantity might be reproduced well while others poorly, so it is always necessary to do initial check calculations when starting to study new systems or old systems with new exchange-correlation functional.

Because of the reasons mentioned above, estimating the errors of the calculation is cumbersome. DFT code GPAW (more in next section) gives errors (with PBE XC functional) in atomization energies and bond lengths of well-known molecules less than one percent. To get good results, the calculations must be converged well enough.

There is a vast number of quantities that cannot be derived from electron gas density. For example calculating the optical absorbance requires information of how the electron gas can be excited. Therefore it is very tempting to use the KS single particle states to approximate the electronic excitations. Unlike the electron density, the states do not correspond to real electronic states even in theory. This being said, in practice analyzing them often offers great help, and for example the states near the Fermi level have been successfully correlated with STM-images.[68]

The more rigorous way to study excitations in the system is via time-dependent density functional theory (TD-DFT).[69] There are two approaches to the TD-DFT: real-time propagation of the wave functions[70] and linear response approximation[71]. I will not go into details of these methods, but I want to point out that, as in ground state DFT, where we need to approximate the exchange-correlation functional, in TD-DFT we have to approximate the response functional, which tells how the wave functions response to external electric fields.

2.4.6 The DFT code GPAW

The program I have been mainly using in my research is open source DFT package GPAW (Grid-based projector-augmented wave method).[65, 72, 73] As the name suggests, GPAW uses primarily a uniform real-space grid to represent the wave functions and the electron gas density, and implements the PAW formalism to handle the atomic core regions. Also the LCAO mode has been implemented[74], and at the time of writing this thesis the implementation of plane waves basis set has been also started. GPAW is very versatile program with tested PAW setups available for various elements, and it can be efficiently parallelized over thousand CPUs (with large systems). There is a possibility to do time-dependent DFT (either by using linear response or time propagation)[75], transport calculations and much more. The GPAW is used as an calculator, that is attached to the simulation cell from the ASE package.

2.5 Density-functional tight-binding

Density-functional tight-binding (DFTB) is an approximation to the Kohn-Sham approach of the DFT. In DFTB we use extremely small localized atomic orbital basis to represent wave functions. Distinction to standard DFT is that here we calculate all the integrals needed in evaluating the Hamiltonian and overlap of the

wave functions beforehand and during the actual simulation we simply read and interpolate the integrals from the tables. The exchange-correlation effects are not calculated explicitly but incorporated into the parametrizations beforehand. I will next briefly go through the main points of this method. The notation here differs slightly from the ref. 80 and is hopefully even more clear.

The total energy of the system can be written in a form

$$\begin{aligned} E[n] = \sum_i f_i \left\langle \psi_i \right| -\frac{1}{2}\nabla^2 \left| \psi_i \right\rangle + \int_1 v_{\text{ext}}(\vec{r}_1) n(\vec{r}_1) \\ + \frac{1}{2}\int_1\int_2 \frac{n(\vec{r}_1)n(\vec{r}_2)}{|\vec{r}_2 - \vec{r}_1|} + E_{\text{XC}}[n] + E_{\text{II}}, \end{aligned} \tag{30}$$

where the first term is the kinetic energy T_{s} of the non-interacting electrons, second the potential energy due to external potential, third the Coulombic interaction energy, fourth the exchange-correlation energy, and E_{II} the repulsion energy between the ions. It is the same as equation (20) with the kinetic energy written differently and with the E_{II} term. We then make an approximation that the ground state density n_{min} is close to the density n_0, which we would get if the neutral atoms were brought together and they would not interact with each other. In other words

$$n_{\text{min}} = n_0 + \delta n, \tag{31}$$

where the minimum electron density is calculated as in DFT

$$n_{\text{min}}(\vec{r}) = \sum_i f_i \left| \psi_i(\vec{r}) \right|^2 . \tag{32}$$

where δn is small perturbation to the density n_0. As an example the electron densities of isolated gold atoms and a gold dimer, calculated using DFT, are shown in figure 6. From figure 6e it can be seen that the difference δn between the two densities is rather small.

Then we expand the terms w.r.t. the δn to second order (see appendix A for details) to obtain

$$\begin{aligned} E[n_{\text{min}}] \approx \sum_i f_i \left\langle \psi_i \right| -\frac{1}{2}\nabla^2 + v_{\text{ext}} + v_{\text{H}}[n_0] + v_{\text{XC}}[n_0] \left| \psi_i \right\rangle \\ + \frac{1}{2}\int_1\int_2 \left(\frac{\delta^2 E_{\text{XC}}[n_0]}{\delta n(\vec{r}_1)\delta n(\vec{r}_2)} + \frac{1}{|\vec{r}_2 - \vec{r}_1|} \right) \delta n(\vec{r}_1)\delta n(\vec{r}_2) \\ + E_{\text{XC}}[n_0] - \int_1 v_{\text{XC}}[n_0](\vec{r}_1)\, n_0(\vec{r}_1) - \frac{1}{2}\int_1 v_{\text{H}}[n_0](\vec{r}_1)\, n_0(\vec{r}_1) + E_{\text{II}}. \end{aligned} \tag{33}$$

The first term is called the band structure energy,

$$E_{\text{BS}}[n_{\text{min}}] = \sum_i f_i \left\langle \psi_i \right| \hat{H}_0 \left| \psi_i \right\rangle , \tag{34}$$

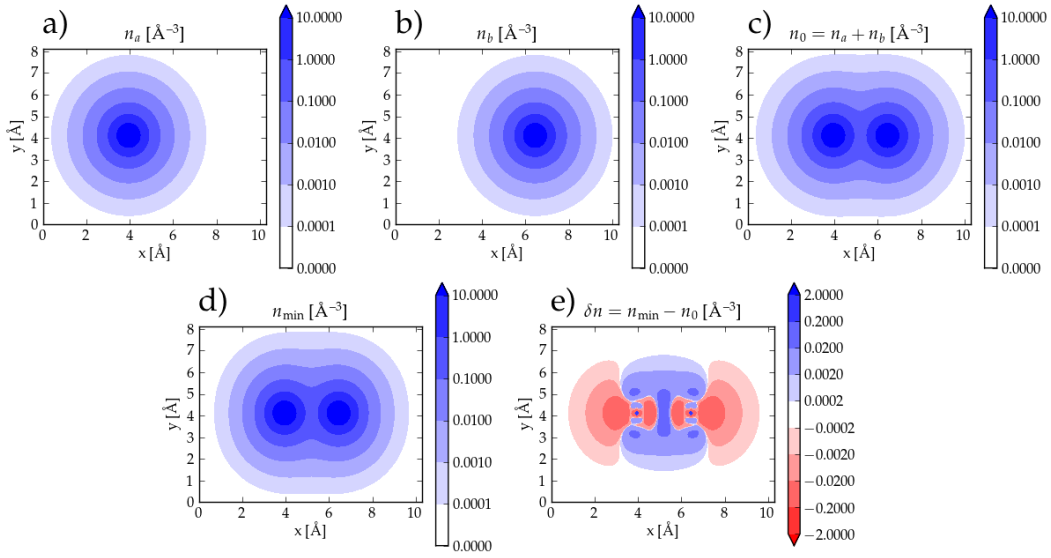

Figure 6: The cross sections ($z = 0$) of the isolated gold atoms and gold dimer electron densities. Panels a and b show the electron densities of isolated gold atom at positions $\vec{R}_a$ and $\vec{R}_b$, respectively. Panel c shows the sum of the densities shown in panels a and b. In panel d is shown the electron density of gold dimer obtained from GPAW grid calculation. Panel e shows the difference between the densities shown in panels c and d. In this case the interaction between the two atom drains the electron density from behind the atoms into the bonding region between the atoms.

in which the Hamiltonian operator $\hat{H}_0$ does not contain any charge transfer effects. The second term takes into account the charge fluctuations in the system:

$$E_{\mathrm{Coul}}[n_0] = \frac{1}{2}\int_1\int_2 \left(\frac{\delta^2 E_{\mathrm{XC}}[n_0]}{\delta n(\vec{r}_1)\delta n(\vec{r}_2)} + \frac{1}{|\vec{r}_2 - \vec{r}_1|}\right)\delta n(\vec{r}_1)\delta n(\vec{r}_2)\ . \tag{35}$$

All the remaining terms are gathered under one object, called the repulsion term

$$E_{\mathrm{rep}} = E_{\mathrm{XC}}[n_0] - \int_1 \left(v_{\mathrm{XC}}[n_0](\vec{r}_1) - \frac{1}{2}v_{\mathrm{H}}[n_0](\vec{r}_1)\right) n_0(\vec{r}_1) + E_{\mathrm{II}}\ . \tag{36}$$

Note that this term does not depend on the charge perturbation δn.

Tight-binding is very broad concept, and it has been used successfully before.[76–79] I will now dig into how to calculate the three energy terms in practice.

2.5.1 The band structure energy

As stated before, we use minimal localized atomic basis. The atom-centered orbitals ϕ_i are constructed from real combinations of spherical harmonics, multiplied by radial functions:

$$\phi_i(\vec{r}) = R_i(r)Y_i(\hat{r}), \tag{37}$$

where R_i is the radial function for state i and Y_i is a real combination of spherical harmonics with proper angular momentum for the state i. The radial functions are obtained from DFT calculation of an isolated atom with added confinement potential v_{conf} to make the wave functions less diffuse:

$$\Big\{ -\frac{1}{2}\nabla^2 + v_{\text{s}} + v_{\text{conf}} \Big\}\phi_i = \varepsilon_i \phi_i. \tag{38}$$

We have used quadratic form for the confinement

$$v_{\text{conf}}(r) = \left(\frac{r}{r_0}\right)^2, \tag{39}$$

where r_0 is one of the parameters. The default is to set $r_0 = 2 \cdot r_{\text{cov}}$, where r_{cov} is the covalent radius of the element. Minimal basis also means that we have only one radial function for each angular momentum l. Each element has at least one s-type basis function. For some elements (e.g. hydrogen) this is adequate. The basis set can be enhanced by adding three p-type orbitals (good for e.g. carbon). For transition metal elements with weakly bound valence electrons we can have in addition five d-type orbitals. All of the basis functions are visualized in table 2 of ref. 80.

We use these localized basis function to expand the KS states

$$|\psi_i\rangle = \sum_\mu c_{i\mu} |\phi_\mu\rangle , \tag{40}$$

where the μ goes through every atomic orbital at every atom. The band structure energy becomes

$$E_{\text{BS}} = \sum_i f_i \langle\psi_i| \hat{H}_0 |\psi_i\rangle = \sum_i f_i \sum_\mu \sum_\nu c^*_{i\mu} c_{i\nu} \underbrace{\langle\phi_\mu| \hat{H}_0 |\phi_\nu\rangle}_{=H^0_{\mu\nu}} . \tag{41}$$

2.5.2 The charge fluctuation term

The charge fluctuation is decomposed into localized atomic contributions, that are approximated by a Gaussian distribution (this approximation is justified in figure 1

of ref. 80). If we further assume that the exchange-correlation part is only local (i.e. we ignore the XC effects of the charges between different atoms), we can write

$$\frac{1}{2}\int_1\int_2 \frac{\delta n(\vec{r}_1)\delta n(\vec{r}_2)}{|\vec{r}_2-\vec{r}_1|} \approx \frac{1}{2}\sum_{I,J}^{\text{atoms}} \Delta q_I \Delta q_J \, \gamma_{IJ}, \tag{42}$$

where

$$\gamma_{IJ} = \begin{cases} U_I, & I = J \\ \frac{\text{erf}(C_{IJ}R_{IJ})}{R_{IJ}}, & I \neq J \end{cases} \tag{43}$$

and

$$\Delta q_I = \sum_i f_i \sum_{\mu\in I}\sum_\nu \frac{1}{2}\left(c^*_{i\mu}c_{i\nu} + c.c.\right) S_{\mu\nu} - q^0_I \ . \tag{44}$$

The parameter U_I is the on-site energy of the charge fluctuation at atom I, and it contains both Coulombic and XC energies. The default value for the U_I is to calculate the ionization energy minus the electron affinity:

$$U_I = IE - EA, \tag{45}$$

where the IE and EA are determined by DFT calculations. By default the parameters C_{IJ} are defined by the parameters U_I of the atoms. Because with local XC functional there are no long-range effects, the parameters C_{IJ} can be tuned if needed.

The Δq_I represents the extra charge on the atom I. The $S_{\mu\nu}$ is the overlap matrix of the orbitals ϕ_μ an ϕ_ν, and q^0_I is the number of valence electrons on the neutral atom I. The equation follows from the assumption that integrating the overlap of two orbitals (ϕ_μ at site I and ϕ_ν at site J) over the volume belonging to the atom I can be approximated by half of the overlap of these orbitals over the whole space, i.e.

$$\int_{V_I} \phi_\mu(\vec{r})\phi_\nu(\vec{r}) \approx \frac{1}{2}\int \phi_\mu(\vec{r})\phi_\nu(\vec{r}) = \frac{1}{2}S_{\mu\nu}. \tag{46}$$

This is called Mulliken population analysis.

With these approximations the Coulombic and XC energy due to charge fluctuations is easy and fast to calculate. However, including these effects often increases the calculation time considerably because more iterations are needed to get a converged result.

2.5.3 The repulsion term

The biggest contribution to this term is the ion-ion repulsion (hence the name), but it also contain all the errors we have made in the approximations so far. Because

we don't know how to treat all the parts in this term, the repulsion term is simply fitted to some reference systems. The total repulsive energy in the system is then

$$E_{\text{rep}} = \sum_I \sum_{J>I} V_{\text{rep}}^{IJ}(R_{IJ}), \tag{47}$$

where R_{IJ} is the distance of the atoms I and J and V_{rep}^{IJ} is the repulsive energy between them. The functions V_{rep}^{IJ} are fitted for each element pair separately.

We produce the repulsion potential by fitting a smoothing spline to the collected data points. There is one parameter λ that defines how smooth the fitted curve is, and another R_{cut} that defines the range of the repulsion.

These terms must be short-ranged for them to be transferable, so they cannot be used to compensate all the errors we have made before. The default strategy is to choose a set of reference systems (e.g. small molecules, bulk material) and optimize the bond lengths or lattice constant by tuning the fitting parameters. The parametrization process for thiolate-protected gold clusters is shown in chapter 3.1.1.

2.5.4 Calculating the ground state

We have now derived the equation for the total energy of the system as

$$\begin{aligned} E &= E_{\text{BS}} + E_{\text{Coul}} + E_{\text{rep}} \\ &= \sum_i f_i \sum_\mu \sum_\nu c_{i_\mu}^* c_{j\nu} H_{\mu\nu}^0 + \frac{1}{2} \sum_{I,J}^{\text{atoms}} \Delta q_I \Delta q_J \gamma_{IJ} + \sum_I \sum_{J>I} V_{\text{rep}}^{IJ} \ . \end{aligned} \tag{48}$$

Then we apply the variation principle $\delta(E - \sum_i \varepsilon_i \langle\psi_i|\psi_i\rangle)$ and solve the Lagrange free multipliers for the set of equations

$$\sum_\mu c_{i\mu}^* \left(H_{\mu\nu} - \varepsilon_i S_{\mu\nu}\right) = 0 \ . \tag{49}$$

The overlap matrix elements are integrals

$$S_{\mu\nu} = \int_1 \phi_\mu(\vec{r}_1 - \vec{v}_\mu)\, \phi_\nu(\vec{r}_1 - \vec{v}_\nu) \ . \tag{50}$$

The main idea of the DFTB is to calculate these matrix elements beforehand. This is done by first translating the coordinate system so that the ϕ_μ is at the origin, and then rotating the coordinate system so that the ϕ_ν is at the z-axis:

$$S_{\mu\nu} = \int_1 \varphi_\mu(\vec{r}_1)\, \varphi_\nu(\vec{r}_1 - v\hat{z}), \tag{51}$$

where φ:s are the rotated basis functions, $\vec{v} = \vec{v}_\mu - \vec{v}_\nu$ and $v = |\vec{v}|$ (figure 7a-c). Now, due to the completeness of the spherical harmonics, the rotated basis functions φ can be again expressed as linear combinations of the original basis functions ϕ (figure 7d):

$$\begin{aligned} S_{\mu\nu} &= \int_1 \left(\sum_i a_{\mu i} \phi_i(\vec{r}_1) \right) \left(\sum_j a_{\nu j} \phi_j(\vec{r}_1 - v\hat{z}) \right) \\ &= \sum_i \sum_j a_{\mu i} a_{\nu j} \int_1 \phi_i(\vec{r}_1)\, \phi_j(\vec{r}_1 - v\hat{z}), \end{aligned} \tag{52}$$

where the coefficients a depend on the rotations, i.e. on the vector $\vec{v}$. The summations go over the basis functions at the same atom with same angular momentum (for example the rotated p_x orbital can be expressed as a linear combination of the original p_x, p_y and p_z orbitals).

Here I only talked about overlap matrix elements, but the Hamiltonian matrix elements $H_{\mu\nu}$ in equation (49) are calculated in the similar manner. The catch is that *all* the integrals needed during the simulations can be transformed in a similar way. Most of the integrals in the summation in eq. (52) are zero, and many of the remaining ones are the same. The non-zero integrals are listed in table 3 of ref. 80. Only one of the each symmetrical combinations are shown, naturally e.g. the integral between two p_y orbitals is the same as between the shown p_x orbitals.

As there is only a limited number of orbital pairs that give non-zero integrals, and the integrals only depend on the distance of the orbitals, they can be tabulated beforehand and then simply interpolated during the actual simulations. This gives a huge speed-up to the calculations.

The coefficients $a_{\mu i} a_{\nu j}$ for the integrals are listed in table 4 of ref. 80. I will show how to derive them in appendix B.

2.6 DFTB implementation: `hotbit`

The DFTB method has been implemented in open-source python package `hotbit`. It uses ASE to store the atomic coordinates (as does GPAW) so it is simple to switch between different levels of theory. This enables e.g. quick initial structure optimization using `hotbit`, and then refining the results with GPAW.

All the boundary conditions that can be used with GPAW are implemented also into `hotbit`. In addition, there are e.g. mirror and rotational symmetries available[81], which would be difficult to implement into uniform real-space codes.

Prior to performing calculations, all the needed elements and element pairs have to be parametrized. We have included all the parametrization tools into the `hotbit` code. As explained before, for the repulsive part some reference systems are

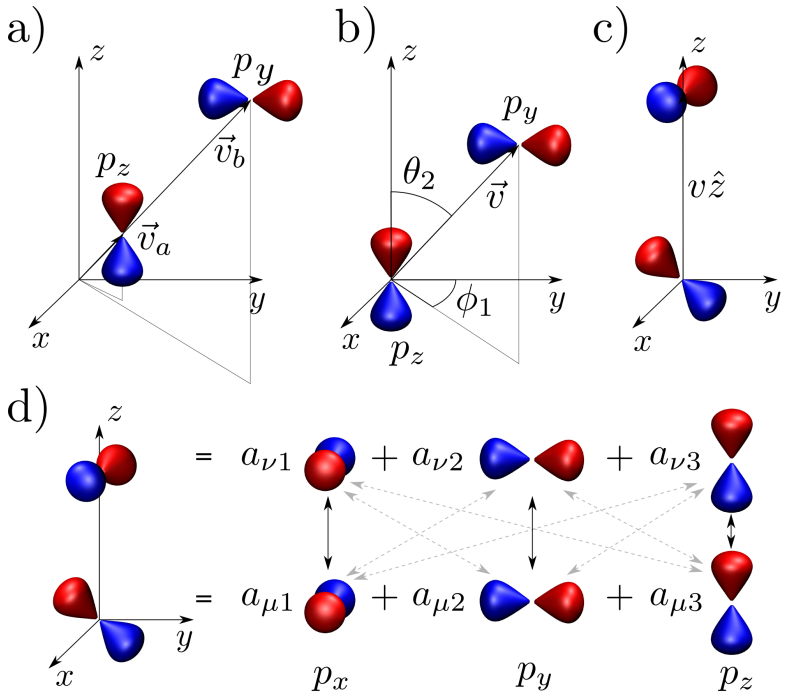

Figure 7: The schematics of the Slater-Koster integral transformations. We want to perform overlap integral of the basis functions p_z at $\vec{v}_a$ and p_y at $\vec{v}_b$ (a). First we translate the system by $-\vec{v}_a$ (b) and rotate (c) so that the one basis function is at the origin and the second on z-axis. Finally we expand the rotated basis functions in new basis (d). The arrows show all the integrals after the expansion. The grey color indicates that the integral is zero by symmetry.

required. They can be systems calculated with e.g. DFT or experimental ground state configurations.

2.7 Molecular dynamics simulations

As already stated before, we are using the Born-Oppenheimer approximation, which means that the movement of the electrons and the nuclei are decoupled. The most common way to do molecular dynamics (MD) simulations is not to simulate the movement of the electrons explicitly, but assume that they are always in the ground state in the external potential created by the moving nuclei.

Prior to performing MD simulations one must choose how to simulate the atomic interactions. The requirement from the method is that it must provide the forces acting on the atoms consistently. All of the previously mentioned methods are able to do this.

There are many different flavours of MD simulations. One straightforward approach is to conserve the total energy of the system. This is called the micro-canonical ensemble or NVE ensemble, where letters refer that the particle number N, simulation cell volume V, and the total energy E are conserved. This is also technically easy because we don't need to worry about adding(removing) particles to(from) the system. In this method we simply calculate the forces f_i acting on the atoms and then propagate them by integrating the classical equations of motion:

$$\begin{aligned} a_i^{(0)} &= \frac{1}{m} f_i^{(0)} \\ x_i^{(1)} &= x_i^{(0)} + v^{(0)}\Delta t + \frac{1}{2} a_i^{(0)} (\Delta t)^2 \\ v_i^{(1)} &= v_i^{(0)} + a_i^{(0)}\Delta t, \end{aligned} \tag{53}$$

where x is the position, v the velocity and a the acceleration of the atom i. The upper indices refer to the instant of time, so the values at time $t + \Delta t$ are obtained by integrating the equations at time t by interval Δt. In practice this straightforward method leads to large errors that quickly accumulate during the subsequent integrations and more advanced (integration) schemes are developed (e.g. velocity-Verlet algorithm[82]), but I will not dig into them.

Here I want to point out that it is important that the accuracy criteria of the electronic structure calculation is high enough. When simply optimizing the structure one ends up very close to the "real" ground state even with quite loose convergence criteria. However, using the same criteria in the MD simulations easily results to a considerable drift of the total energy. Therefore the convergence criteria must be higher than might seem reasonable at the first glance.

The NVE simulation is a very well defined way to do MD. However, it leads to the kinematics where the temperature is not constant, especially in systems with small number of atoms. This is natural since temperature is a thermodynamical quantity that is properly defined only for macroscopic system. Thus in small systems there can be substantial fluctuations in such quantities. As a simple example, one liter of hydrogen gas can have steady temperature, but the kinetic energy of a particular H_2 molecule varies substantially as a function of time.

Another way to do MD simulations is canonical ensemble, NVT. Here, instead of conserving the total energy, the method tries to keep the temperature constant. This can be achieved in many ways and maybe the most famous way is to use the Langevin equation, where we add extra "noise" to the forces we get from the ground state calculation:

$$a_i^{(0)} = \frac{1}{m} f_i^{(0)} + \mu_i \ . \tag{54}$$

The nature of noise term μ_i is random so the NVT MD simulation are non-deterministic and depending on how the noise forces are generated the simulations

can also be non-reproducible. In any case there is no good physical argument to decide which way is the best, and therefore the arguments for NVT simulation are flimsy. As can be seen from the previous hydrogen example, especially in small systems constant temperature would be even non-physical.

There are other approaches, where e.g. the size of the simulation cell may vary in order to keep pressure constant. Independent of the chosen flavor of molecular dynamics simulation, the main procedures are more or less the same:

1. Put atoms into the simulation cell to initial coordinates.
2. Calculate the forces acting on the ions (if e.g. DFT or DFTB is used, then this means solving the electronic structure for the current atomic configuration).
3. Propagate atoms according to Newton's 2nd law for previously determined time step.
4. Stop simulation or return to step 2.

2.7.1 Structure optimization

Usually we are interested in the ground state configuration of the system. Finding the energy minimum of the system is a two-sided problem. Finding a local minimum is done simply by incorporating the idea of MD simulation, but instead of moving the particles according to the Newtonian laws, we simply move them along the force vectors, and repeat until the residual forces are small enough. We may end up to the global minimum if the initial atomic configuration was close to the real ground state.

The problem is that often the atomic systems have many metastable configurations[83], and the optimization algorithm might get trapped into one of those. To circumvent this, more sophisticated structure optimization algorithms have been developed, for example simulated annealing method, where the system is heated in order to escape the metastable states, or genetic algorithms, which try to find the optimal configuration by joining and mutating randomly created initial atomic configurations.[84–87] As the number of atoms increases, it becomes impossible to search the whole configuration space, and one can never be sure whether the structure the algorithm finds is the most optimal one.

3 Results

3.1 Modeling thiolate-protected gold clusters with density-functional tight-binding

The theoretical prediction of the structure of thiolate-protected clusters from scratch is extremely difficult. If certain mass and composition have been measured, it allows us to concentrate on a smaller configuration space. However, clusters with more than 30 gold atoms are already demanding systems for DFT and a faster method would be extremely useful. The classical force fields are not accurate enough for these systems because the electronic structure, which is an important stabilizing factor, is not incorporated in the method. Therefore we turned our attention to the DFTB since in this method the electronic effects are taken into account explicitly.

With DFTB we can access not only the atomic configuration but also some electronic properties, e.g. charge transfer in the system. We used the atomic and electronic structure as the indicators for the validity of our parametrizations. We were not expecting 100 % agreement with experimental or DFT results, but qualitative agreement so that we could use DFTB to quickly identify promising structure candidates and then switch to DFT for more accurate analysis.

3.1.1 Creating the parametrizations

First we needed to parametrize the important interactions. In this case we needed interactions for Au–Au, Au–S, S–C and C–H element pairs. Of course in general all the interactions are important, but in this study only the above mentioned chemical bonds exist in the clusters (with SCH_3 ligands), and other chemical bonds do not play any role.

As explained before, the parametrizations contain physically three different parts. First in the parametrization process one must construct the wave functions for the isolated atoms with additional confinement potential defined by the parameter r_0 (see equation (39)). This defines the band structure part of the total energy. We used the default value for the confinement potential parameter r_0, as I found that these systems (or at least the properties we were looking at) are quite insensitive to this parameter.

The next parameter to define is the Coulombic energy and the parameter U in equation (45). We again used the default values for all the elements.

The last term in the total energy expression is the repulsive energy. After all the other parameters are fixed, the repulsive potential is fitted to minimize the difference between the DFTB and some reference systems. The repulsive term affects directly only the geometry, so it is natural to try to minimize the difference of the atomic positions.

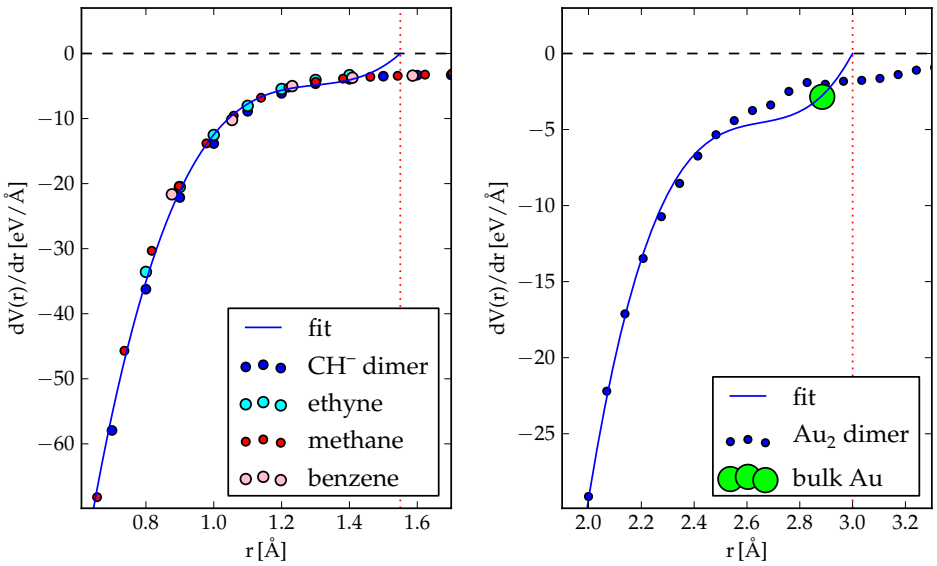

Figure 8: Fitting the repulsive forces for the C−H (a) and Au−Au (b) interaction. The points show the deviations in the forces of the DFT and DFTB calculations without the repulsive potential. The red dotted lines indicate the cut radii for the repulsions.

The reference systems and the process of parametrizations for the thiolate-protected gold clusters are discussed in the ref. [88]. In short, to parametrize the Au–S, S–C and C–H interactions we used several small molecules. With our parametrizations the geometries of these molecules were accurately reproduced. For the Au–Au we tried several reference systems with varying luck. The DFT optimized Au_{55} clusters tended to distort with DFTB. In the end using the gold dimer and bulk gold gave the best results. The problems in parametrizing this specific interaction hints that because the Au–Au interactions is metallic, it is difficult to describe it using a minimal basis set employed in DFTB. This is seen in the comparison of the fits of the repulsive potentials for the C−H and Au−Au in figure 8. For the C−H repulsion several molecules give similar data points, which hints that the parametrization is transferable. In the case of Au−Au, the dimer curve and bulk gold data point differ substantially, which means that the Au−Au parametrization may not work in all the systems with the same accuracy. Note that the both curves are not close to zero at the cut distance. This hints that there are long-range effects that are not completely described by the band structure and Coulombic terms.

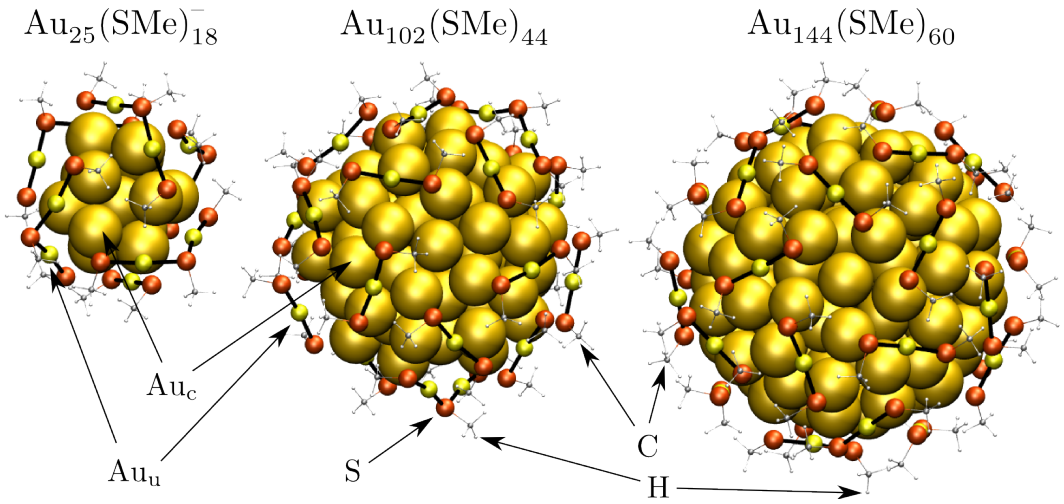

Figure 9: The three thiolate-protected clusters with methyl groups as the ligands in the units. The two Au atoms refer to gold atoms in the core (Au_c) and in the units (Au_u).

We did not deliberately design our parametrizations only for protected gold clusters but since we used known clusters as benchmark systems, the obtained parametrizations are of course implicitly biased to some extent.

3.1.2 The simulations

We applied our new parametrizations to three thiolate-protected gold clusters $Au_{25}(SR)^-_{18}$, $Au_{102}(SR)_{44}$ and $Au_{144}(SR)_{60}$, shown in figure 9. For the first two there is experimentally resolved atomic structure, for the third only theoretical model exists so far. We compared the DFTB relaxed atomic configurations to the DFT ones by measuring the distance of the atoms from the center of mass of the cluster. In these clusters the atoms form "shells" which are seen as spikes in figure 10. In this sense the atomic configurations were well reproduced, the clusters did not distort extensively and the similar atomic shell structure is observable in both calculations. The DFTB is not perfect; for example in figure 10c) the 3rd and 4th shell join into one shell. The symmetry, however, is preserved in all three cases.

The positions of the thiolates at the gold surface are not random, but each has specific location so that the whole surface of the core is passivated. This is important for the stability of the cluster. The gold-thiolate interface is accurately reproduced by the DFTB and our parametrizations. The units bond to the same gold atoms as in the experimental structure, and even the different Au−S bond lengths are reproduced, as can be seen in the table 1 (note that we use same

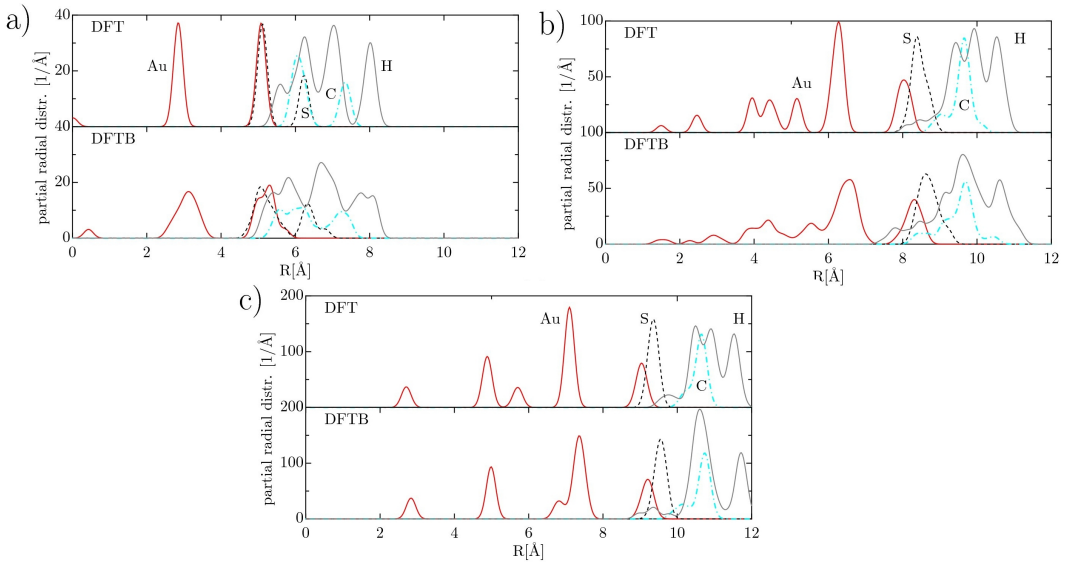

Figure 10: The radial distribution of the atoms of three different thiolate-protected gold clusters, calculated with DFT and DFTB. a) $Au_{25}(SMe)^{-}_{18}$ b) $Au_{102}(SMe)_{44}$ c) $Au_{144}(SMe)_{60}$.

parametrizations for all the elements, i.e. we do not have separate parametrizations for gold atoms in the core and in the protecting units).

The comparison of charge transfer in different methods is not straightforward. In DFT the excess charges on the atoms are often calculated using the Bader method. In DFTB we get the charge of the atom from Mulliken analysis.[80] Keeping in mind that the whole definition of which portion of the electron gas belongs to which atom is arbitrary to high degree, comparing the numbers from different simulation methods with different analysis methods very strictly is not reasonable. We calculated the charge transfer using GPAW in both grid mode (to get Bader charges) and in LCAO mode with different basis sets (to get Mulliken charges) in order to make better comparison. This is shown in table II. in ref. [88]. The results vary to some extent but the general trends are similar.

The electronic structure is well reproduced. The clear angular momentum character of the electronic states and the state separations near the Fermi energy are quite comparable to the DFT results, as can be seen from figure 11. With DFTB the symmetry of the clusters is slightly distorted and therefore the degeneracies of some of the states are broken, and in the largest cluster the state ordering is not exactly the same. The explanation might be that in larger clusters the electronic structure is not as important as in the small ones, and the errors in the Au−Au parametrization accumulate and overcome the electronic effects that try to preserve

Table 1: The Au-S bond lengths in three thiolate-protected clusters, calculated with DFT and DFTB.

		Au_c-S (Å)	Au_u-S (Å)
$Au_{25}(SMe)^-_{18}$	DFT	2.400 ± 0.039	2.344 ± 0.004
	DFTB	2.407 ± 0.017	2.378 ± 0.004
$Au_{102}(SMe)_{44}$	DFT	2.448 ± 0.035	2.348 ± 0.012
	DFTB	2.519 ± 0.292	2.379 ± 0.006
$Au_{144}(SMe)_{60}$	DFT	2.463 ± 0.013	2.339 ± 0.004
	DFTB	2.418 ± 0.004	2.377 ± 0.002

symmetry.

In this work we concentrated on the gold core and the gold-thiolate layer of the clusters, and we used methyl groups as the ligands in the protecting layer. We managed to produce parametrizations that reproduce the geometries and electronic structures quite well. However, more tests and different benchmarks are required to gain better understanding of the reliability of these parametrizations. Already at this point the DFTB (and our parametrizations) could be used in studies where the ligand layer is modified, since the DFTB reproduces the geometry of the gold-thiolate interface well and organic molecules are an ideal target for tight-binding methods.

3.2 Thermal behaviour of $Au_{25}(SH)^-_{18}$

The $Au_{25}(SR)^-_{18}$ cluster has been shown experimentally to work as a catalyst in room temperature solution for hydrogenating aldehydes and ketones.[89] However, at the atomic level the reaction is not understood. The reactive gold core is covered by the protecting units, so it should not be able to react with anything. One possible explanation is that the units vibrate in such a fashion that sometimes the gold core is exposed for a short period of time. We decided to tackle this problem with molecular dynamics simulations.

To produce a reliable trajectory using MD simulation the potential energy surface (especially around the equilibrium configuration) should be well reproduced. Because we do not have well established understanding of the strengths and weaknesses of DFTB and our parametrizations, we decided to use DFT in LCAO mode for this study. We ran four 10 ps long NVE molecular dynamics simulations in approximately 300 K, 400 K, 500 K and 600 K temperatures. As explained before, in NVE simulation the temperature cannot be controlled exactly, as so the average temperatures of the simulations turned out to be 304 K, 392 K, 495 K and 596 K,

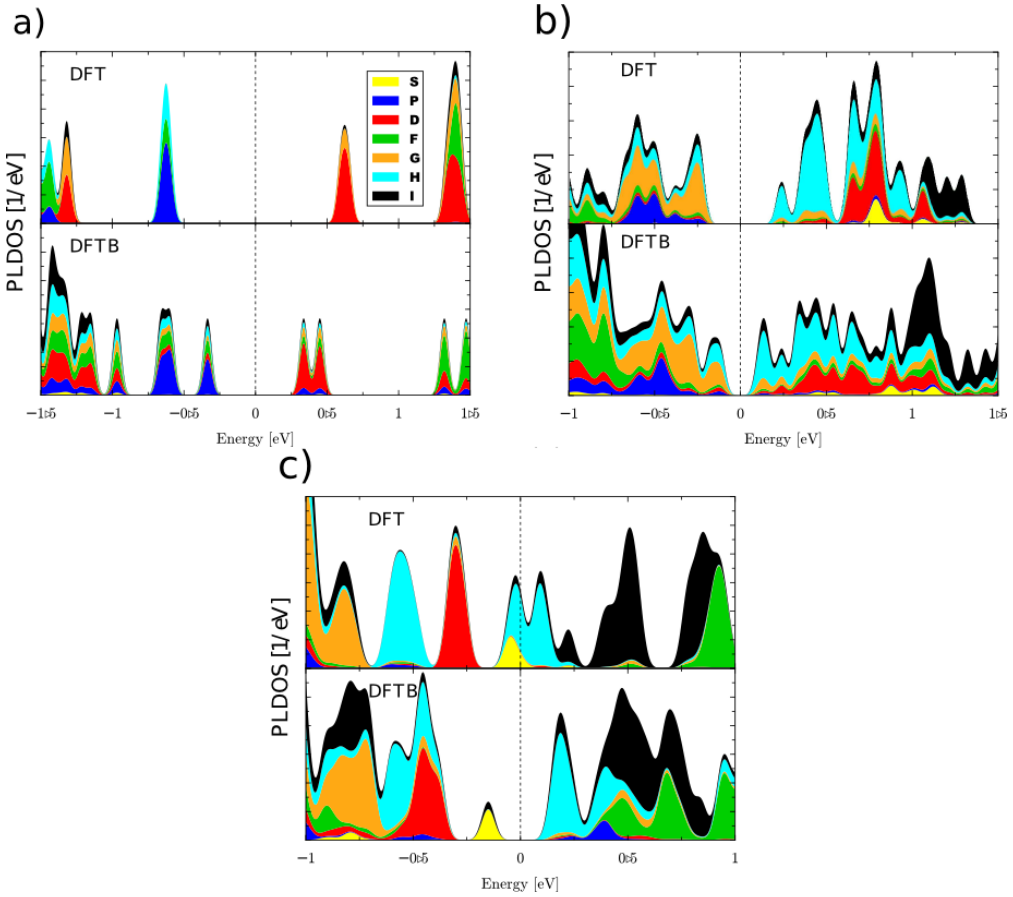

Figure 11: The angular momentum character of the Kohn-Sham states from DFT and DFTB calculations. a) $Au_{25}(SMe)^-_{18}$ b) $Au_{102}(SMe)_{44}$ c) $Au_{144}(SMe)_{60}$. The Fermi energy is set to zero in each panel.

with standard deviations of roughly 8 %.

We found out that the structure of the cluster is surprisingly stable. In ground state configuration the atoms are located at specific distances, or shells, from the center of mass, and this feature is prominent even at 600 K temperature, see figure 12. The thermal vibrations of course broaden the sharp ground state peaks but the shells structure is clearly seen at all temperatures. Judging by the maxima of the peaks there is slight thermal expansion in the cluster. The heat capacity, which is the derivative of the total energy with respect to the temperature (the slope of the graph in figure 13), stays the same in all the temperatures we studied. This indicates that the cluster is not close to melting.

The $Au_{25}(SR)^-_{18}$ cluster contains only long V-shaped protecting units, so each

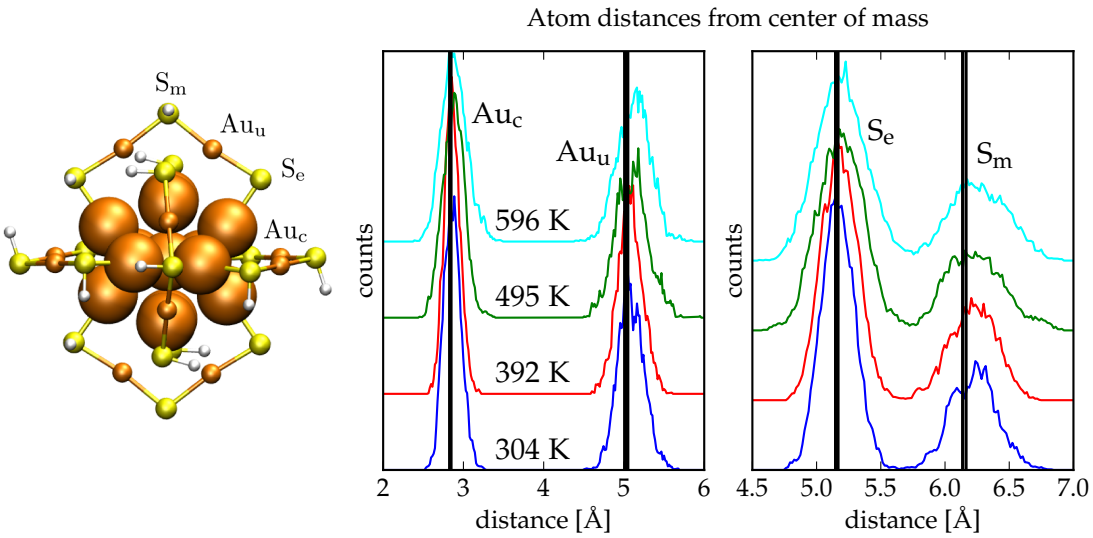

Figure 12: Left: The model cluster $Au_{25}(SH)^-_{18}$ used in this study. Some of the atoms are named for further analysis. Right: The radial atomic distributions in different temperatures. Black lines indicate 0 K positions.

unit contains three ligands. In the experimentally resolved structure the ligands at the end of the units always point to opposite directions. This is probably the configuration where the ligands feel the least steric repulsion from each other. In our model we passivated the sulfur atoms simply with hydrogen atoms pointing to the same directions as the real ligands. Naturally hydrogens do not see each other, so in principle they could be able to flip to point to opposite direction. However, during the 10 ps simulations we did not observe a single flip, which hints that already the electronic structure alone keeps the orientation of the ligands ridig. Because the real ligands cannot vibrate freely due to the steric repulsion and they might be even bound together via van der Waals forces (e.g. via π-stacking[30]), it is unlikely that there is any ligand flipping taking place in real clusters either.

We analyzed the bond length distributions in the cluster to get information about the strengths of the bonds. The distributions are shown in figure 14. The shape of the distribution of the Au–S bonds in the protecting units is symmetric, which suggests that the bonds are vibrating in the harmonic region and are not close to breaking. In contrast, the distribution of the Au–S bonds between the sulfur atoms at the end of the units and the core gold atoms are asymmetric, suggesting that the vibration is already anharmonic. This hints that these bonds are the weakest and may be the first to break in longer simulations or higher temperatures.

The zero Kelvin atomic structure of the cluster atoms is highly symmetric. This imposes symmetry also to the electronic structure and the states near the

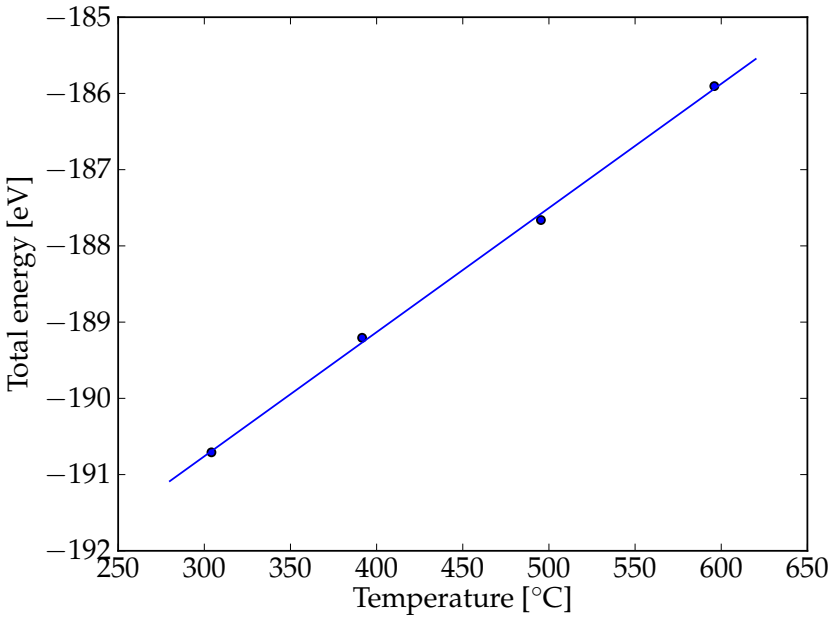

Figure 13: The average total energy of the cluster as a function of temperature. The slope of the fit gives the heat capacity.

Fermi energy have distinct angular momentum character. The HOMO is threefold degenerate with p-type symmetry, the LUMO is twofold degenerate with d-type symmetry. In addition the HOMO-LUMO gap is over 1 eV. These effects further stabilize the cluster. We studied how much the electronic structure is affected as the thermal movement breaks the high symmetry of the 0 K structure.

Both the HOMO and LUMO notably broaden (i.e. the degeneracy is broken) compared to the 0 K values and the broadening slightly increases as a function of temperature. Also the HOMO-LUMO gap narrows as the temperature increases. The gap is, however, over 1 eV in all the simulations. The angular momentum characteristics of the HOMO and LUMO states are conserved. This indicates that the superatom model is valid at room temperatures and participates in stabilizing the cluster.

In our simulations we did not observe any phenomena that would explain the catalytic behaviour of the cluster. The protecting units stay at their very places during the whole simulations and the core is never exposed. It is of course possible that our simulations were too short and that eventually we would observe something that offers an explanation for the catalysis. Another possibility is that the catalytic reaction is more complex and involves solvent molecules and perhaps

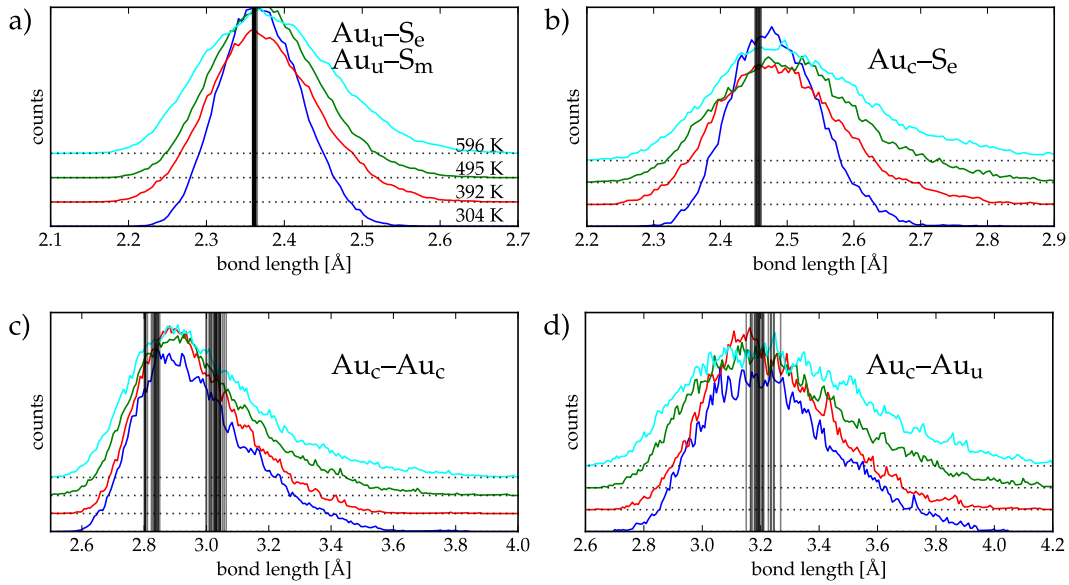

Figure 14: The bond length distributions of the Au−S and Au−Au bonds in $Au_{25}(SH)^-_{18}$ in different temperatures. The black vertical lines indicate the bonds at 0 K.

several reacting molecules.

3.3 Modeling the coating of titanium dioxide and dye adsorption

So far the systems studied have been so small that it has been possible to include the whole particle into the simulation (albeit with smaller ligands). This changes in the case of dye-sensitized solar cells.

This study was conducted in a collaboration with experimental groups, that tried to improve the efficiency of DSSCs by coating the titanium dioxide with a thin layer of aluminum oxide prior to attaching the dye molecules. They employed ALD method to grow the coating layer by using trimethyl aluminum (TMA, $Al(CH_3)_3$) and water as precursors. We studied the formation of the aluminum oxide layer and its effect on the adsorption of the dye molecules by modeling them both with DFT.

The general structure of the DSSC is explained in section 1.3. The porous titanium dioxide on the anode is often prepared by sintering together TiO_2 nanoparticles, in which the anatase is the prevailing crystal structure. These are too large to be simulated with reasonable resources. Therefore we applied the normal procedure

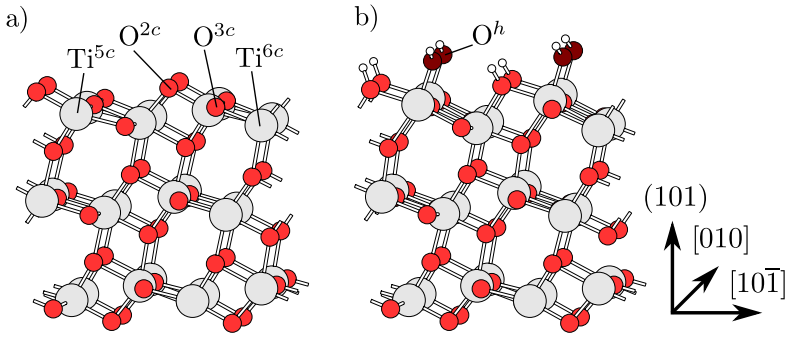

Figure 15: The clean (a) and hydrated (b) TiO_2 anatase (101) surface. The atoms names in panel a indicate the coordination number of the titanium and oxygen atoms, and in panel b the h refers to hydration.

to simulate only the surface of these particles with the help of periodic boundary conditions.

As can be seen from e.g. STM images[90] in anatase nanoparticles the (101) surface is the most exposed one due to it being energetically the most favoured one. Therefore the natural choice was to model the TiO_2 surface in the DSSCs with anatase (101) surface. We intentionally ignored other surfaces, crystal defects, terraces etc. and concentrated on the most stable facet on the TiO_2 anatase nanocrystal. Taking into account all the possible surfaces and numerous defects would render the problem too complex to tackle.

In this the GPAW program package was again employed, this time with the grid basis. We calculated the bulk anatase unit cell to be $3.82\,\text{Å} \times 9.57\,\text{Å}$ which is in good agreement with experimental and other theoretical results.[91, 92] Next we built a three-layer thick stoichiometric (101) slab to model the surface. The model is shown in figure 15a. Three layers is the thinnest that produces reasonable density of states.[40, 93, 94]

In the ALD process prior to the first ALD cycle the surface is exposed to water vapor, and H_2O supposedly dissociates to form OH groups and hydrogens to surface titanium and oxygen atoms, respectively. As there is no proper understanding of how large portion of the surface is hydrated at these temperatures[95], we put the maximal coverage of the OH-groups on the surface to get the upper limit for the Al_2O_3 coverage after the first ALD cycle (figure 15b).

We modeled the first cycle of the ALD process, where the aluminum oxide was grown on TiO_2 anatase(101) with precursor molecules H_2O and $Al(CH_3)_3$ (trimethyl aluminum, TMA). The ALD cycle is a two-step process, which can be

expressed as the following two reactions

$$\begin{aligned} \mathrm{TiOH^{*}} + \mathrm{Al(CH_3)_3} &\rightarrow \mathrm{TiOAl(CH_3)^{*}_{3-n}} + n \cdot \mathrm{CH_4} \\ \mathrm{Al(CH_3)^{*}_{3-n}} + (3-n) \cdot \mathrm{H_2O} &\rightarrow \mathrm{Al(OH)^{*}_{3-n}} + (3-n) \cdot \mathrm{CH_4} \end{aligned} \tag{55}$$

The first reaction describes the adsorption of the TMA molecule on the hydrated surface. It can bind by losing one methyl group ($n = 1$ in the equation), which we called single ligand exchange adsorption, or two methyl groups ($n = 2$), in which case we called it double ligand exchange adsorption. The size of our surface model is such that the maximum number of TMA molecules that can be adsorbed is four. In the second reaction the adsorbed TMA molecules are exposed to vapor. In the reaction the H_2O dissociates and forms methane gas with the methyl groups of the aluminum atoms.

The adsorption energy of a TMA molecule was calculated using the equation

$$E_{\mathrm{ads}} = E_{\mathrm{surf+TMA}} - E_{\mathrm{surf}} - E_{\mathrm{TMA}}, \tag{56}$$

where, $E_{\mathrm{surf+TMA}}$ is the total energy of the surface with TMA adsorbed, E_{surf} is the total energy of the hydrated surface, and E_{TMA} is the total energy of the TMA in gas phase. The negative adsorption energy means that the adsorption is exothermic.

For single ligand-exchange adsorption we found three competing sites, and for double ligand-exchange four sites were identified. These are shown in figure 16 with the corresponding adsorption energies. We developed a labeling scheme for the adsorptions. The names of the surface atoms related to the adsorption are separated by dashes. In single ligand-exchange adsorption two surface atoms are involved and one donates a hydrogen. With double ligand-exchange adsorption three atoms are involved, and two donate hydrogen atoms. Therefore in our labeling the first or two first names indicate the surface atoms that donate hydrogens.

We estimated the surface coverage by calculating the differential adsorption energies for the adding of TMAs. The adsorption energy for the $\mathrm{N^{th}}$ TMA is calculated from the equation

$$E^{N}_{\mathrm{diff.ads.}} = E^{N}_{\mathrm{surf}} + x \cdot E_{\mathrm{CH_4}} - E^{N-1}_{\mathrm{surf.}} - E_{\mathrm{TMA}}, \tag{57}$$

where E^{N}_{surf} is the total energy of a surface with N TMAs, $E_{\mathrm{CH_4}}$ and E_{TMA} the gas phase energies of methane and TMA, respectively, and x is 1 for a single and 2 for double ligand-exchange adsorption. We concentrated only on adsorptions h-h, 2c-h and h-2c-h. Our calculations show that via single ligand-exchange adsorption three TMA molecules may adsorb on the surface, the third with half of the adsorption energy of the first two. In addition the third TMA rotates on the surface, and effectively blocks the fourth TMA from adsorbing. If forced on the surface, the

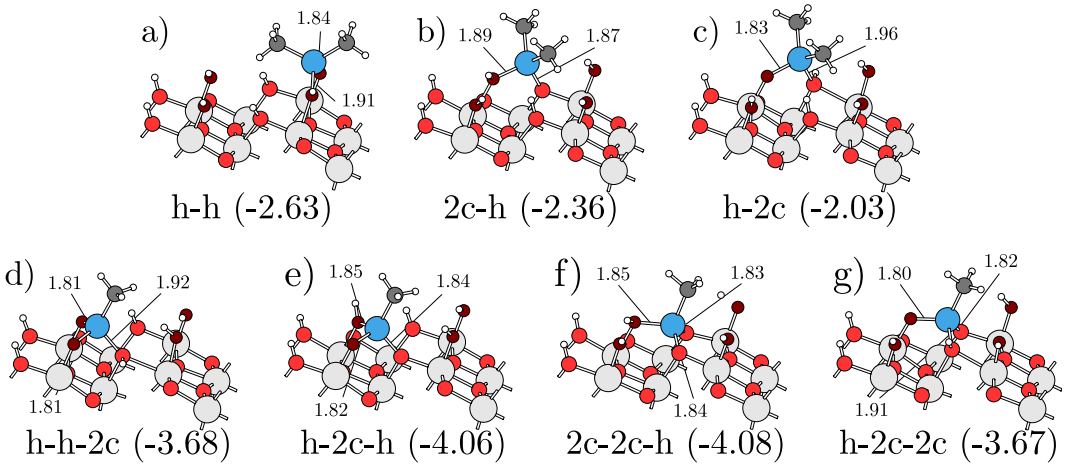

Figure 16: The three single (a-c) and four double (d-e) ligand-exchange adsorption geometries found in this work. The names indicate to which atoms the aluminum atom is binding (see figure 15 for the names). The adsorption energies are shown after the names (in electronvolts).

binding of fourth TMA is energetically neutral. With double ligand-exchange binding four TMAs can be adsorbed with similar energies.

We explained the difference by the steric repulsion of the methyl groups. In the single ligand-exchange case the third TMA rotates on the surface in order to maximize the distances between the methyl groups. With double ligand-exchange this is not a problem, because each adsorbed TMA has only one methyl group attached. Based on the binding energies we estimated the maximum methyl group surface density to be 0.5 ML to 0.75 ML, or 5.1 nm^{-2} to 7.6 nm^{-2}. This is in accordance with an estimation for the maximum methyl group surface density 7.2 nm^{-2} given in ref. 47. Also the TMA (or aluminum atom) surface density from our calculations was in good agreement with TOF-ERD measurements.[96] Because the adsorption energies of different adsorption geometries are so similar, it is fair to assume that the structure of the initial ALD layer is amorphous.

The obtained surface aluminum density suggests that the coating after the first ALD cycle does not completely cover the TiO_2 surface, but some areas are left exposed to the electrolyte in the cell. The electrolyte used in the DSSC often contains iodine, where it exist in I_2 and I_3^- forms.[97] As the I_3^- is linear, we studied whether it is able to penetrate the porous AlO layer by forcing an iodine atom to the surface. Our calculations showed that there is virtually no barrier for an iodine atom to adsorb from the gas phase to the TiO_2 surface through the hole in the aluminum oxide layer (see figure 17).

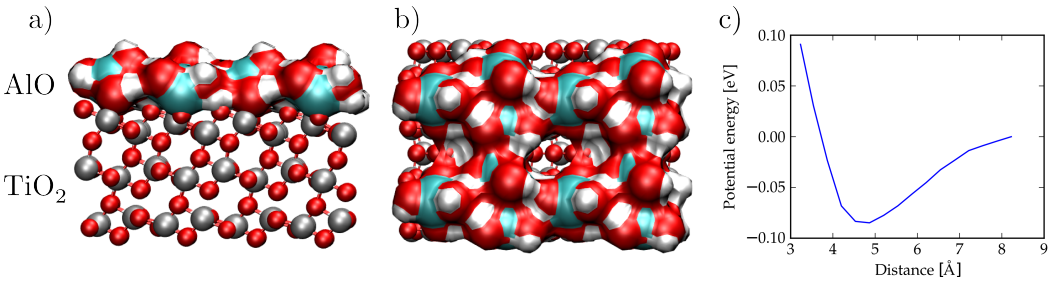

Figure 17: Panels a and b show side and top views of the original TiO_2 slab (balls and sticks) and the 0.75 ML AlO coating (surface). The top view shows the hole in the coating. In panel c is plotted the total energy of the slab and an iodine atom as a function of the distance of the atom from the highest Ti atoms on top of the hole.

Next, we studied how the coating affects the binding of the most common dye molecule N3. Binding on the clean anatase (101) surface has been studied extensively[38–40] with DFT, which gave us a good starting point and ideas for the binding geometries on the coating. We chose to study the surface with three TMAs adsorbed via h-h single ligand-exchange adsorption (with methyl groups replaced by OH groups). This surface we call OH-rich. In experiments the coated TiO_2 is often heated in order to remove excess water from the surface. Therefore we used also another surface model, called OH-deficient, which is the OH-rich surface with one OH group removed from each aluminum and the same number of hydrogen atoms from the surface.

The best adsorption geometry on the clean surface (from ref. 40) and three adsorptions on the coated surface we found are shown in figure 18. Our calculations suggest that already after the first ALD cycle the N3 cannot anymore bind to the original TiO_2 surface due to steric repulsion and is therefore forced to bind on the new aluminum oxide coating. This lifts the molecule at least 1.7 Å, almost doubling the adsorption distance from the clean surface, so the electron injection rate is inevitably decreased. This, with the fact that it is possible that the electron-electrolyte recombination may not be completely hindered, raises serious doubts about enhancing the efficiency of the DSSCs via aluminum oxide coating.

We also studied the beginning of the second ALD cycle to find out whether the holes in the coating could be filled in subsequent ALD cycles. Replacement of the methyl groups with OH groups should be independent of each other, i.e. if one can be replaced then they all will be. Therefore we modeled the first half of the second cycle by simply replacing the methyl groups with OH ones. We studied four different adsorption sites for the first TMA of the second cycle. We found out

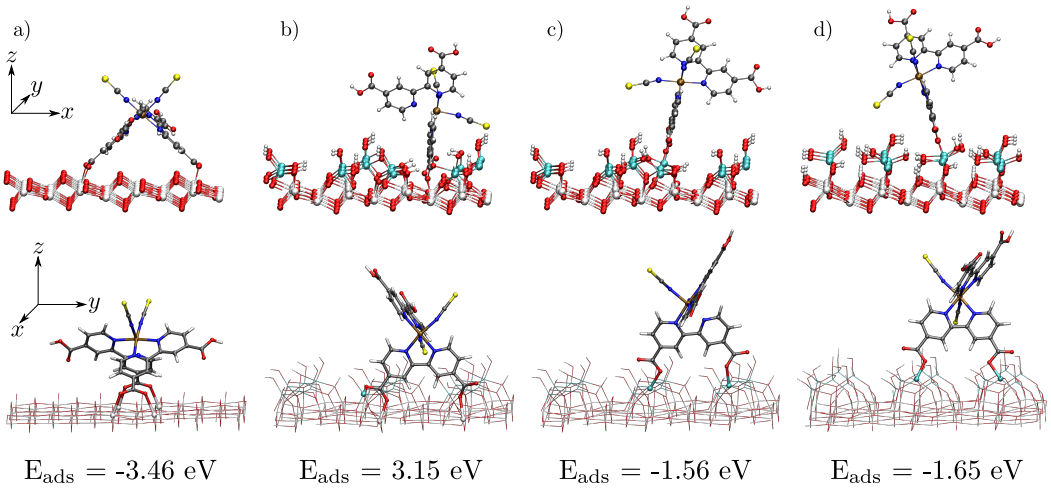

Figure 18: The different adsorption geometries of the N3 dye molecule. Panel a shows the optimal adsorption geometry on the clean anatase (101) surface (according to ref. 40). Panels b and c show the adsorptions on the OH-deficient surface. In panel b the N3 is connected to the TiO_2 whereas in panel c it binds to the aluminum atoms. In panel d the adsorption on the OH-rich surface is shown.

that there is no big difference whether the TMA adsorbs on the original TiO_2 or on the new aluminum oxide. This indicates that the holes can be filled in the later ALD cycles but also that the surface can be quite rough after few cycles.

Our results are based on the calculated thermodynamical properties (total energy differences) and kinetic effects (e.g. reaction barriers) are ignored. There is evidence that in real situation both adsorption mechanisms take place.[98] The small size of our unit cell places restrictions on the accuracy of the surface cover estimation. We used ideal anatase (101) surface to model the surface of the TiO_2 nanoparticle. While it is arguably decent model for the surface, not all the details (defects, terraces etc.) are taken into account. Therefore our results are suggestive. However, as the methyl group surface density seems to be the limiting factor for the adsorption of TMA molecules, one can assume that similar results can be obtained also from other surface models.

4 Summary and outlook

In the nanoscale systems the exact knowledge of atomic and electronic structure is important for understanding the properties of the systems. Even small structural differences may result into very different properties. Solving the complete quantum-mechanical problem, however, is impossible, and some approximations must be used. I have used two tools, the density-functional theory, which is nowadays widely used standard tool for theoretical physicists and chemists, and the density-functional tight-binding, which can be used to solve the electronic and atomic structure.

The thiolate-protected gold cluster $Au_{25}(SR)_{18}^{-}$ was studied by density functional theory molecular dynamics simulations. We were able to identify that the weakest point in the cluster is the gold-thiolate interface, judging by the anharmonic bond length profile. Also the explanations for the stability (the symmetric atomic and electronic configuration) hold in the presence of thermal vibrations. Our results can help to explain other mysteries concerning the cluster, e.g. how it works as a catalyst.

We were also able to employ the density-functional tight-binding to study thiolate-protected gold cluster by developing parametrization for the needed chemical interactions. The work can help to eventually simulate these particles with considerably less computational resources, even though at this point more benchmarking is still needed to get better understanding on the reliability of the method.

The properties of thiolate-protected gold clusters must be studied more, their properties understood better, and their handling improved before they are ready to be used in applications. The situation is different with dye-sensitized solar cells. They have been actively developed since their introduction by Grätzel, and research is needed mainly to enhance their efficiency and stability. The efficiency has been tried to improve by coating the titanium dioxide in the cells with aluminum oxide to prevent the electrolyte reaching the TiO_2. Our simulations suggest that the forming AlO layer does not prohibit this completely, but at the same time it does weaken the electron injection rate from the dye to TiO_2 by lifting the dye molecules further away from the surface.

These two research subjects I have been involved with are quite different in many aspects. Despite the completely different nature of these systems the same computational methods can be used to describe and simulate them. This shows that the methods are quite universal and highly adaptable to different problems. Therefore their development is important to the nanoscience. As the commercial electronic devices get smaller and smaller, also the fruits of the nanoscience research become more comprehensible to the layman in the form of e.g. faster and smaller electronic devices.

References

[1] Classical element. http://en.wikipedia.org/wiki/Classical_element

[2] J. J. Thomson Biography. http://www.nobelprize.org/nobel_prizes/physics/laureates/1906/thomson-bio.html

[3] Ernest Rutherford Biography. http://www.nobelprize.org/nobel_prizes/chemistry/laureates/1908/rutherford-bio.html

[4] ATLAS and the Higgs. http://www.atlas.ch/news/2012/atlas-and-the-higgs.html

[5] CERN experiments observe particle consistent with long-sought Higgs boson. http://press.highenergyphysicsmedia.com/2/post/2012/07/cern-experiments-observe-particle-consistent-with-long-sought-higgs-boson1.html

[6] *M. Haruta.* **Catalysis: Gold rush**. Nature **437**, 1098 (2005).

[7] *G. J. Hutchings.* **Vapor-Phase Hydrochlorination of Acetylene - Correlation of Catalytic Activity of Supported Metal Chloride Catalysts**. J. Catal. **96**, 292 (1985).

[8] *B. Hvolbaek, T. V. W. Janssens, B. S. Clausen, H. Falsig, C. H. Christensen and J. K. Norskov.* **Catalytic activity of Au nanoparticles**. Nano Today **2**, 14 (2007).

[9] *S. Loth, S. Baumann, C. P. Lutz, D. M. Eigler and A. J. Heinrich.* **Bistability in Atomic-Scale Antiferromagnets**. Science **335**, 196 (2012).

[10] *A. Lechtken, C. Neiss, J. Stairs and D. Schooss.* **Comparative study of the structures of copper, silver, and gold icosamers: Influence of metal type and charge state**. J. Chem. Phys. **129**, 154304 (2008).

[11] *Y. Q. Wang, W. S. Liang and C. Y. Geng.* **Coalesce Behavior of Gold Nanoparticles**. Nanoscale Res. Lett. **4**, 684 (2009).

[12] *F. Marano, S. Hussain, F. Rodrigues-Lima, A. Baeza-Squiban and S. Boland.* **Nanoparticles: molecular targets and cell signalling**. Archives of Toxicology **85**, 733 (2011).

[13] *L. C. Kennedy, L. R. Bickford, N. A. Lewinski, A. J. Coughling, Y. Hu, E. S. Day, J. L. West and R. A. Drezek.* **A New Era for Cancer Treatment: Gold-Nanoparticle-Mediated Thermal Therapies**. Small **7**, 169 (2011).

[14] *A. Retnakumari, S. Setua, D. Menon, P. Ravindran, H. Muhammed, T. Pradeep, S. Nair and M. Koyakutty.* **Molecular-receptor-specific, non-toxic, near-infrared-emitting Au cluster-protein nanoconjugates for targeted cancer imaging**. Nanotechnology **21**, 055103 (2010).

[15] *X. Qian, X. Peng, D. O. Ansari, Q. Yin-Goen, G. Z. Chen, L. Yang, A. N. Young, M. D. Wang and S. Nie.* **In vivo tumor targeting and spectroscopic detection with surface-enhanced Raman nanoparticle tags**. Nature Biotechnology **26**, 83 (2008).

[16] *P. Frondelius, H. Häkkinen and K. Honkala.* **Adsorption and activation of O_2 at Au chains on MgO/Mo thin films**. Phys. Chem. Chem. Phys. **12**, 1483 (2010).

[17] *C. E. Briant, B. R. C. Theobald, J. W. White, L. K. Bell, D. M. P. Mingos and A. J. Welch.* **Synthesis and X-ray structural characterization of the centred icosahedral gold cluster compound $[Au_{13}(PMe_2Ph)_{10}Cl_2](PF_6)_3$; the realization of a theoretical prediction**. J. Chem. Soc., Chem. Commun. **5**, 201 (1981).

[18] *M. Brust, M. Walker, D. Bethell, D. J. Schiffrin and R. Whyman.* **Synthesis of Thiol-derivatised Gold Nanoparticles in a Two-phase Liquid-Liquid System**. J. Chem. Soc., Chem. Commun. **7**, 801 (1994).

[19] *P. D. Jadzinsky, G. Calero, C. J. Ackerson, D. A. Bushnell and R. D. Kornberg.* **Structure of a Thiol Monolayer-Protected Gold Nanoparticle at 1.1 Å Resolution**. Science **318**, 430 (2007).

[20] *M. Walter, J. Akola, O. Lopez-Acevedo, P. D. Jadzinsky, G. Calero, C. J. Ackerson, R. L. Whetten, H. Grönbeck and H. Häkkinen.* **A unified view of ligand-protected gold clusters as superatom complexes**. Proc. Natl. Acad. Sci. USA **105**, 9157 (2008).

[21] *M. W. Heaven, A. Dass, P. S. White, K. M. Holt and R. W. Murray.* **Crystal Structure of the Gold Nanoparticle $[N(C_8H_{17})_4][Au_{25}(SCH_2CH_2Ph)_{18}]$**. J. Am. Chem. Soc. **130**, 3754 (2008).

[22] *M. Z. Zhu, C. M. Aikens, F. J. Hollander, G. C. Schatz and R. C. Jin.* **Correlating the Crystal Structure of A Thiol-Protected Au_{25} Cluster and Optical Properties**. J. Am. Chem. Soc. **130**, 5883 (2008).

[23] *M. Z. Zhu, W. T. Eckenhoff, T. Pintauer and R. C. Jin.* **Conversion of anionic $[Au_{25}(SCH_2CH_2Ph)_{18}]^-$ cluster to charge neutral cluster via air oxidation**. J. Phys. Chem. C **112**, 14221 (2008).

[24] *H. F. Qian, W. T. Eckenhoff, Y. Zhu, T. Pintauer and R. C. Jin.* **Total Structure Determination of Thiolate-Protected Au(38) Nanoparticles**. J. Am. Chem. Soc. **132**, 8280 (2010).

[25] *M. Z. Zhu, H. F. Qian and R. C. Jin.* **Thiolate-Protected Au(20) Clusters with a Large Energy Gap of 2.1 eV**. J. Am. Chem. Soc. **131**, 7220 (2009).

[26] *H. F. Qian, Y. Zhu and R. C. Jin.* **Isolation of Ubiquitous $Au_{40}(SR)_{24}$ Clusters from the 8 kDa Gold Clusters**. J. Am. Chem. Soc. **132**, 4583 (2010).

[27] *A. Dass.* **Mass Spectrometric Identification of $Au_{68}(SR)_{34}$ Molecular Gold Nanoclusters with 34-Electron Shell Closing**. J. Am. Chem. Soc. **131**, 11666 (2009).

[28] *A. Dass.* **Faradaurate Nanomolecules: A Superstable Plasmonic 76.3 kDa Cluster**. J. Am. Chem. Soc. **133**, 19259 (2011).

[29] *O. Lopez-Acevedo, J. Akola, R. L. Whetten, H. Grönbeck and H. Häkkinen.* **Structure and Bonding in the Ubiquitous Icosahedral Metallic Gold Cluster $Au_{144}(SR)_{60}$**. J. Phys. Chem. C **113**, 5035 (2009).

[30] *C. L. Heinecke, T. W. Ni, S. Malola, V. Mäkinen, O. A. Wong, H. Häkkinen and C. J. Ackerson.* **Structural and Theoretical Basis for Ligand Exchange on Thiolate Monolayer Protected Gold Nanoclusters**. J. Am. Chem. Soc. **134**, 13316 (2012).

[31] Enerdate - global energy intelligence. `http://www.enerdata.net`

[32] NASA: GISS Surface Temperature Analysis (GISTEMP). `http://data.giss.nasa.gov/gistemp`

[33] *B. C. O'Regan and M. Grätzel.* **A low-cost, high-efficiency solar-cell based on dye-sensitized colloidal TiO_2 films**. Nature **353**, 737 (1991).

[34] *A. Hagfeldt, G. Boschloo, L. Sun, L. Kloo and H. Petterson.* **Dye-Sensitized Solar Cells**. Chem. Rev. **110**, 6595 (2010).

[35] *S. Ardo and J. Meyer.* **Photodriven heterogeneous charge transfer with transition-metal compounds anchored to TiO_2 semiconductor surfaces**. Chem. Soc. Rev. **38**, 115 (2009).

[36] *C. Chen, N. Pootrakulchote, M-Y. Chen, T. Moehl, H-H. Tsai, S. M. Zakeeruddin, C. Wu and M. Grätzel.* **A New Heteroleptic Ruthenium Sensitizer for Transparent Dye-Sensitized Solar Cells**. Adv. Energ. Mater. **2**, 1503 (2012).

[37] Solar Technologies Analysis. `http://www.nrel.gov/analysis/pubs_solar.html`

[38] *F. De Angelis, S. Fantacci, A. Selloni, M. K. Nazeeruddin and M. Grätzel.* **First-Principles Modeling of the Adsorption Geometry and Electronic Structure of Ru(II) Dyes on Extended TiO_2 Substrates for Dye-Sensitized Solar Cell Applications**. J. Phys. Chem. C **114**, 6054 (2010).

[39] *F. De Angelis, S. Fantacci, A. Selloni, M. K. Nazeeruddin and M. Grätzel.* **Time-Dependent Density Functional Theory Investigations on the Excited States of Ru(II)-Dye-Sensitized TiO_2 Nanoparticles: The Role of Sensitizer Protonation**. J. Am. Chem. Soc. **129**, 14156 (2007).

[40] *F. Schiffmann, J. VandeVondele, J. Hutter, R. Wirz, A. Urakawa and A. Baiker.* **Protonation-Dependent Binding of Ruthenium Bipyridyl Complexes to the Anatase(101) Surface**. J. Phys. Chem. C **114**, 8398 (2010).

[41] *F. Schiffmann, J. VandeVondele, J. Hutter, A. Urakawa, R. Wirz and A. Baiker.* **An atomistic picture of the regeneration process in the dye sensitized solar cells**. Proc. Natl. Acad. Sci. USA **107**, 4830 (2010).

[42] *V. Ganapathy, B. Karunagaran and S. Rhee.* **Improved performance of dye-sensitized solar cells with TiO_2/alumina core-shell formation using atomic layer deposition**. J. Power Sourc. **195**, 5138 (2010).

[43] *L. J. Antila, M. J. Heikkilä, V. Aumanen, M. Kemell, P. Myllyperkiö, M. Leskelä and J. E. I. Korppi-Tommola.* **Suppression of Forward Electron Injection from $Ru(dcbpy)_2(NCS)_2$ to Nanocrystalline TiO_2 Film As a Result of an Interfacial Al_2O_3 Barrier Layer Prepared with Atomic Layer Deposition**. J. Phys. Chem. Lett. **1**, 536 (2010).

[44] *G. Wahl, P. B. Davies, R. F. Bunshah, B. A. Joyce, C. D. Bain, G. Wegner, M. Remmers, F. C. Walsh, K. Hieber, J-E. Sundgren, P. K. Bachmann, S. Miyazawa, A. Thelen and H. Strathmann.* **Thin Films**. Ullmann's Encyclopedia of Industrial Chemistry **36**, 519 (2012).

[45] *L. L. Hench and J. K. West.* **The Sol-Gel Process**. Chem. Rev. **90**, 33 (1990).

[46] *S. M. George.* **Atomic Layer Deposition: An Overview**. Chem. Rev. **110**, 111 (2010).

[47] *R. L. Puurunen.* **Surface chemistry of atomic layer deposition: A case study for the trimethylaluminum/water process**. J. Appl. Phys. **97**, 121301 (2005).

[48] *Y. Widjaja and C. B. Musgrave.* **Quantum chemical study of the mechanism of aluminum oxide atomic layer deposition**. Appl. Phys. Lett. **80**, 3304 (2002).

[49] *C. Mui, Y. Widjaja, J. K. Kang and C. B. Musgrave.* **Surface reaction mechanisms for atomic layer deposition of silicon nitride**. Surf. Sci. **557**, 159 (2004).

[50] *J. H. Han, G. Gao, Y. Widjaja, E. Garfunkel and C. B. Musgrave.* **A quantum chemical study of ZrO_2 atomic layer deposition growth reactions on the SiO_2 surface**. Surf. Sci. **550**, 199 (2004).

[51] *Z. Hu and C. H. Turner.* **Initial Surface Reaction of TiO_2 Atomic Layer Deposition into SiO_2 Surfaces: Density Functional Theory Calculations**. J. Phys. Chem. B **110**, 8337 (2006).

[52] *J. T. Tanskanen, J. R. Bakke, S. F. Bent and T. A. Pakkanen.* **Molecular Level Insights into Atomic Layer Deposition of CdS by Quantum Chemical Calculations**. J. Phys. Chem. C **114**, 16618 (2010).

[53] *M. Nolan and S. D. Elliott.* **Competing Mechanisms in Atomic Layer Deposition of Er_2O_3 versus La_2O_3 from Cyclopentadienyl Precursors**. Chem. Mater. **22**, 117 (2010).

[54] *A. B. Mukhopadhyay, C. B. Musgrave and J. Fdez. Sanz.* **Atomic Layer Deposition of Hafnium Oxide from Hafnium Chloride and Water**. J. Am. Chem. Soc. **130**, 11996 (2008).

[55] *S. D. Elliott and H. P. Pinto.* **Modelling the Deposition of High-k Dielectric Films by First Principles**. J. Electroceram. **13**, 117 (2004).

[56] *A. Heyman and C. B. Musgrave.* **A quantum chemical study of the atomic layer deposition of Al_2O_3 using $AlCl_3$ and H_2O as precursors**. J. Phys. Chem. B **108**, 5718 (2004).

[57] *V. V. Brodskii, E. A. Rykova, A. A. Bagatur'yants and A. A. Korkin.* **Modelling of ZrO_2 deposition from $ZrCl_4$ and H_2O on the Si(100) surface: initial reactions and surface structures**. Comput. Mater. Sci. **24**, 278 (2002).

[58] *G. C. Abell.* **Empirical chemical pseudopotential theory of molecular and metallic bonding.** Phys. Rev. B **31**, 6184 (1985).

[59] *D. J. Griffiths.* **Introduction to Quantum Mechanics, Second Edition**. Pearson Education, Inc. (2005).

[60] *P. Schwerdtfeger.* **Relativistic effects in properties of gold.** Heteroat. Chem. **13**, 578 (2002).

[61] *P. Hohenberg and W. Kohn.* **Inhomogenous Electron Gas**. Phys. Rev. **136**, B864 (1964).

[62] *W. Kohn and L. J. Sham.* **Self-Consistent Equations Including Exchange and Correlation Effects**. Phys. Rev. **140**, A1133 (1965).

[63] Libxc manual. `http://www.tddft.org/programs/octopus/wiki/index.php/Libxc:manual`

[64] *J. P. Perdew, K. Burke and M. Ernzerhof.* **Generalized Gradient Approximation Made Simple**. Phys. Rev. Lett. **77**, 3865 (1996).

[65] *S. R. Bahn and K. W. Jacobsen.* **An object-oriented scripting interface to a legacy electronic structure code**. Comput. Sci. Eng. **4**, 56 (2002).

[66] *S. R. Elliot.* **The Physics and Chemistry of Solids**. Wiley (2005).

[67] *G. Kresse and J. Furthmüller.* **Efficient iteratice schemes for ab initio total-energy calculations using a plane-wave basis set**. Phys. Rev. B **54**, 11169 (1996).

[68] *X. Lin, N. Nilius, H. J. Freund, M. Walter, P. Frondelius, K. Honkala and H. Häkkinen.* **Quantum Well States in Two-Dimensional Gold Clusters on MgO Thin Films**. Phys. Rev. Lett. **102**, 206801 (2009).

[69] *E. Runge and E. K. U. Gross.* **Density-Functional Theory for Time-Dependent Systems.** Phys. Rev. Lett. **52**, 997 (1984).

[70] *K. Yabana and G. F. Bertsch.* **Time-dependent local-density approximation in real time.** Phys. Rev. B **54**, 4484 (1996).

[71] *M. E. Casida* in **Recent Developments and Applications in Modern Density-Functional Theory**, edited by J. M. Seminario (Elsevier, Amsterdam, 1996), p. 391.

[72] *J. J. Mortensen, L. B. Hansen and K. W. Jacobsen.* **Real-space grid implementation of the projector augmented wave method**. Phys. Rev. B **71**, 035109 (2005).

[73] *J. Enkovaara, C. Rostgaard, J. J. Mortensen, J. Chen, M. Dulak, L. Ferrighi, J. Gavnholt, C. Glinsvad, V. Haikola, H. A. Hansen, H. H. Kristoffersen, M. Kuisma, A. H. Larsen, L. Lehtovaara, M. Ljungberg, O. Lopez-Acevedo, P. G. Moses, J. Ojanen, T. Olsen, V. Petzold, N. A. Romero, J. Stausholm-Moller, M. Strange, G. A. Tritsaris, M. Vanin, M. Walter, B. Hammer, H. Häkkinen, G. K. H. Madsen, R. M. Nieminen, J. K. Norskov, M. Puska, T. T. Rantala, J. Schiotz, K. S. Thygesen and K. W. Jacobsen.* **Electronic structure calculations with GPAW: a real-space implementation of the projector augmented-wave method**. J. Phys.: Condens. Matter **22**, 253202 (2010).

[74] *A. H. Larsen, M. Vanin, J. J. Mortensen, K. S. Thygesen and K. W. Jacobsen.* **Localized atomic basis set in the projector augmented wave method.** Phys. Rev. B **80**, 195112 (2009).

[75] *M. Walter, H. Häkkinen, L. Lehtovaara, M. Puska, J. Enkovaara, C. Rostgaard and J. J. Mortensen.* **Time-dependent density-functional theory in the projector augmented-wave method.** J. Chem. Phys. **128**, 244101 (2008).

[76] *Th. Frauenheim, G. Seifert, M. Elstner, Z. Hainal, G. Jungnickel, D. Porezag, S. Suhai and R. Scholz.* **A Self-Consistent Charge Density-Functional Based Tight-Binding Method for Predictive Materials Simulations in Physics, Chemistry and Biology**. Phys. status solidi b **217**, 41 (2000).

[77] *M. Elstner, D. Porezag, G. Jungnickel, J. Elsner, M. Haugk, Th. Frauenheim, S. Suhai and G. Seifert.* **Self-consistent-charge density-functional tight-binding method for simulations of complex materials properties**. Phys. Rev. B **58**, 7260 (1998).

[78] *T. A. Niehaus, S. Suhai, F. D. Sala, P. Lugli, M. Elstner, G. Seifert and Th. Frauenheim.* **Tight-binding approach to time-dependent density-functional response theory**. Phys. Rev. B **63**, 085108 (2001).

[79] *D. Porezag, Th. Frauenheim, Th. Köhler, G. Seifert and R. Kaschner.* **Construction of tight-binding-like potentials on the basis of density-**

functional theory: Application to carbon. Phys. Rev. B **51**, 12947 (1995).

[80] *P. Koskinen and V. Mäkinen.* **Density-functional tight-binding for beginners**. Comput. Mater. Sci. **47**, 237 (2009).

[81] *O. O. Kit, L. Pastewka and P. Koskinen.* **Revised periodic boundary conditions: Fundamentals, electrostatics, and the tight-binding approximation**. Phys. Rev. B **84**, 155431 (2011).

[82] *W. C. Swope, H. C. Andersen, P. H. Berens and K. R. Wilson.* **A computer simulation method for the calculation of equilibrium constants for the formation of physical clusters of molecules: Applications to small water clusters**. J. Chem. Phys. **76**, 637 (1982).

[83] *P. Koskinen, H. Häkkinen, G. Seifert, S. Sanna, Th. Frauenheim and M. Moseler.* **Density-functional based tight-binding study of small gold clusters**. New Journal of Physics **8**, 9 (2006).

[84] *S. M. Woodley and R. Catlow.* **Crystal structure prediction from first principles.** Nature Material **7**, 937 (2008).

[85] *J. J. Zhao and R. H. Xie.* **Genetic Algorithms for the Geometry Optimization of Atomic and Molecular Clusters.** J. Comput. Theor. Nanosci. **1**, 117 (2004).

[86] *C. J. Pickard and R. J. Needs.* **Ab initio random structure searching.** J. Phys.: Condens. Matter **23**, 053201 (2011).

[87] *J. C. Schon, K. Doll and M. Jansen.* **Predicting solid compounds via global exploration of the energy landscape of solids on the ab initio level without recourse to experimental information.** Phys. Status Solidi B **247**, 23 (2010).

[88] *V. Mäkinen, P. Koskinen and H. Häkkinen.* **Modeling thiolate-protected gold clusters with density-functional tight-binding**. Eur. Phys. J. D. *Accepted for publication.*

[89] *Y. Zhu, H. F. Qian, B. A. Drake and R. C. Jin.* **Atomically Precise $Au_{25}(SR)_{18}$ Nanoparticles as Catalysts for the Selective Hydrogenation of α,β-Unsaturated Ketones and Aldehydes**. Angew. Chem. **49**, 1295 (2010).

[90] *W. Hebenstreit, N. Ruzycki, G. S. Herman, Y. Gao and U. Diebold.* **Scanning tunneling microscopy investigation of the TiO_2 anatase (101) surface**. Phys. Rev. B **62**, R16334 (2000).

[91] *J. K. Burdett, T. Hughbanks, G. J. Miller, J. W. Richardson, Jr. and J. V. Smith.* **Structural-Electronic Relationships in Inorganic Solids: Powder Neutron Diffraction Studies of the Rutile and Anatase Polymorphs of Titanium Dioxide at 15 and 295 K**. J. Am. Chem. Soc. **109**, 3939 (1987).

[92] *M. Lazzeri, A. Vittadini and A. Selloni.* **Structure and energetics of stoichiometric TiO_2 anatase surfaces**. Phys. Rev. B **63**, 155409 (2001).

[93] *V. Mäkinen, K. Honkala and H. Häkkinen.* **Atomic Layer Deposition of Aluminum Oxide on TiO_2 and Its Impact on N3 Dye Adsorption from First Principles**. J. Phys. Chem. C **115**, 9250 (2011).

[94] *U. Aschauer, Y. He, H. Cheng, S. Li, U. Diebold and A. Selloni.* **Influence of Subsurface Defects on the Surface Reactivity of TiO_2: Water on Anatase (101)**. J. Phys. Chem. C **114**, 1278 (2010).

[95] *V. E. Henrich and P. A. Cox.* **The Surface Science of Metal Oxides**. Press Syndicate of the University of Cambridge (1994).

[96] *L. J. Antila, M. J. Heikkilä, V. Mäkinen, N. Humalamäki, M. Laitinen, V. Linko, P. Jalkanen, J. Toppari, V. Aumanen, M. Kemell, P. Myllyperkiö, K. Honkala, H. Häkkinen, M. Leskelä and J. E. I. Korppi-Tommola.* **ALD Grown Aluminum Oxide Submonolayers in Dye-Sensitized Solar Cells: The Effect on Interfacial Electron Transfer and Performance**. J. Phys. Chem. C **115**, 16720 (2011).

[97] *M. Grätzel.* **Conversion of sunlight to electric power by nanocrystalline dye-sensitized solar cells**. J. Photoch. Photobio. A **164**, 3 (2004).

[98] *A. Rahtu, T. Alaranta and M. Ritala.* **In Situ Quartz Crystal Microbalance and Quadrupole Mass Spectrometry Studies of Atomic Layer Deposition of Aluminum Oxide from Trimethylaluminum and Water**. Langmuir **17**, 6506 (2001).

A DFT total energy expansion

Functional is a mathematical object that returns a number when it is given a function. They can be Taylor expanded around a function analogously to functions that can be Taylor expanded around a point:

$$F[n_0+\delta n] = F[n_0] + \sum_{k=1}^{\infty} \frac{1}{k!} \int_1 ... \int_k \frac{\delta^k F[n_0]}{\delta n(\vec{r}_1)...\delta n(\vec{r}_k)} \delta n(\vec{r}_1)...\delta n(\vec{r}_k), \tag{58}$$

where

$$\int_1 \frac{\delta F[n_0]}{\delta n(\vec{r}_1)} \delta n(\vec{r}_1) \equiv \lim_{\epsilon \to 0} \frac{1}{\epsilon} \Big[F[n_0 + \epsilon \delta n] - F[n_0] \Big] \ . \tag{59}$$

Writing down the expansion of the Hartree energy to the second order gives

$$E_{\mathrm{H}}[n_0+\delta n] \approx E_{\mathrm{H}}[n_0] + \int_1 \frac{\delta E_{\mathrm{H}}[n_0]}{\delta n(\vec{r}_1)} \delta n(\vec{r}_1) + \frac{1}{2} \int_1 \int_2 \frac{\delta^2 E_{\mathrm{H}}[n_0]}{\delta n(\vec{r}_1) \delta n(\vec{r}_2)} \delta n(\vec{r}_1) \delta n(\vec{r}_2) \ . \tag{60}$$

Using the definition (59) the first term is

$$\begin{aligned}
&\int_1 \frac{\delta E_{\mathrm{H}}[n_0]}{\delta n(\vec{r}_1)} \delta n(\vec{r}_1) = \lim_{\epsilon \to 0} \frac{1}{\epsilon} \Big[E_{\mathrm{H}}[n_0 + \epsilon \delta n] - E_{\mathrm{H}}[n_0] \Big] \\
&= \lim_{\epsilon \to 0} \frac{1}{\epsilon} \left[\frac{1}{2} \int_1 \int_2 \frac{\left(n_0(\vec{r}_1) + \epsilon \delta n(\vec{r}_1)\right) \left(n_0(\vec{r}_2) + \epsilon \delta n(\vec{r}_2)\right)}{|\vec{r}_2 - \vec{r}_1|} - \frac{1}{2} \int_1 \int_2 \frac{n_0(\vec{r}_1) n_0(\vec{r}_2)}{|\vec{r}_2 - \vec{r}_1|} \right] \\
&= \lim_{\epsilon \to 0} \frac{1}{\epsilon} \left[\frac{1}{2} \int_1 \int_2 \left\{ \frac{n_0(\vec{r}_1) n_0(\vec{r}_2)}{|\vec{r}_2 - \vec{r}_1|} + \epsilon \frac{n_0(\vec{r}_1) \delta n(\vec{r}_2)}{|\vec{r}_2 - \vec{r}_1|} + \epsilon \frac{n_0(\vec{r}_2) \delta n(\vec{r}_1)}{|\vec{r}_2 - \vec{r}_1|} \right.\right. \\
&\qquad \left.\left. + \epsilon^2 \frac{\delta n(\vec{r}_1) \delta n(\vec{r}_2)}{|\vec{r}_2 - \vec{r}_1|} - \frac{n_0(\vec{r}_1) n_0(\vec{r}_2)}{|\vec{r}_2 - \vec{r}_1|} \right\} \right] \\
&= \int_1 \int_2 \frac{n_0(\vec{r}_1) \delta n(\vec{r}_2)}{|\vec{r}_2 - \vec{r}_1|} = \int_1 \underbrace{\int_2 \frac{n_0(\vec{r}_2)}{|\vec{r}_2 - \vec{r}_1|}}_{= v_{\mathrm{H}}[n_0](\vec{r}_1)} \delta n(\vec{r}_1) = \int_1 v_{\mathrm{H}}[n_0](\vec{r}_1) \, \delta n(\vec{r}_1).
\end{aligned} \tag{61}$$

We can use this result to calculate the second term:

$$\begin{aligned}
&\frac{1}{2} \int_1 \int_2 \frac{\delta^2 E_{\mathrm{H}}[n_0]}{\delta n(\vec{r}_1) \delta n(\vec{r}_2)} \delta n(\vec{r}_1) \delta n(\vec{r}_2) = \frac{1}{2} \int_1 \frac{\delta}{\delta n(\vec{r}_1)} \int_2 \frac{\delta E_{\mathrm{H}}[n_0]}{\delta n(\vec{r}_2)} \delta n(\vec{r}_2) \delta n(\vec{r}_1) \\
&\quad = \frac{1}{2} \lim_{\epsilon \to 0} \frac{1}{\epsilon} \left[\int_1 \int_2 \frac{n_0(\vec{r}_2) + \epsilon \delta n(\vec{r}_2)}{|\vec{r}_2 - \vec{r}_1|} \delta n(\vec{r}_1) - \int_1 \int_2 \frac{n_0(\vec{r}_2)}{|\vec{r}_2 - \vec{r}_1|} \delta n(\vec{r}_1) \right] \\
&\quad = \frac{1}{2} \int_1 \int_2 \frac{\delta n(\vec{r}_2)}{|\vec{r}_2 - \vec{r}_1|} \delta n(\vec{r}_1) = \frac{1}{2} \int_1 \int_2 \frac{1}{|\vec{r}_2 - \vec{r}_1|} \delta n(\vec{r}_1) \delta n(\vec{r}_2).
\end{aligned} \tag{62}$$

Collecting the results of the expansion of the Hartree energy to the second order, we get

$$E_{\mathrm{H}}[n_0+\delta n] \approx E_{\mathrm{H}}[n_0] + \int_1 v_{\mathrm{H}}[n_0](\vec{r}_1)\,\delta n(\vec{r}_1) + \frac{1}{2}\int_1\int_2 \frac{1}{|\vec{r}_2-\vec{r}_1|}\,\delta n(\vec{r}_1)\delta n(\vec{r}_2)\ . \quad (63)$$

Using the definitions (31) and (32) we can split the second term as

$$\begin{aligned}\int_1 v_{\mathrm{H}}[n_0](\vec{r}_1)\,\delta n(\vec{r}_1) &= \int_1 v_{\mathrm{H}}[n_0](\vec{r}_1)\,n_{\min}(\vec{r}_1) - \int_1 v_{\mathrm{H}}[n_0](\vec{r}_1)\,n_0(\vec{r}_1) \\ &= \sum_i f_i\,\langle\psi_i|\,v_{\mathrm{H}}[n_0]\,|\psi_i\rangle - \int_1 v_{\mathrm{H}}[n_0](\vec{r}_1)\,n_0(\vec{r}_1).\end{aligned} \quad (64)$$

For the exchange-correlation functional we can formally do similar expansion:

$$\begin{aligned}&E_{\mathrm{XC}}[n_0+\delta n] \\ &\quad\approx E_{\mathrm{XC}}[n_0] + \int_1 \frac{\delta E_{\mathrm{XC}}[n_0]}{\delta n(\vec{r}_1)}\delta n(\vec{r}_1) + \frac{1}{2}\int_1\int_2 \frac{\delta^2 E_{\mathrm{XC}}[n_0]}{\delta n(\vec{r}_1)\delta n(\vec{r}_2)}\delta n(\vec{r}_1)\delta n(\vec{r}_2) \\ &\quad= E_{\mathrm{XC}}[n_0] + \int_1 v_{\mathrm{XC}}[n_0](\vec{r}_1)\delta n(\vec{r}_1) + \frac{1}{2}\int_1\int_2 \frac{\delta^2 E_{\mathrm{XC}}[n_0]}{\delta n(\vec{r}_1)\delta n(\vec{r}_2)}\delta n(\vec{r}_1)\delta n(\vec{r}_2) \\ &\quad= E_{\mathrm{XC}}[n_0] + \sum_i f_i\,\langle\psi_i|\,v_{\mathrm{XC}}[n_0]\,|\psi_i\rangle - \int_1 v_{\mathrm{XC}}[n_0](\vec{r}_1)\,n_0(\vec{r}_1) \\ &\qquad+ \frac{1}{2}\int_1\int_2 \frac{\delta^2 E_{\mathrm{XC}}[n_0]}{\delta n(\vec{r}_1)\delta n(\vec{r}_2)}\delta n(\vec{r}_1)\delta n(\vec{r}_2).\end{aligned} \quad (65)$$

B Deriving Slater-Koster transform rules

Let's derive some Slater-Koster transformation rules for the orbitals centered at $\vec{v}_a$ and $\vec{v}_b$ (see figure 7a). The orbitals we use are radial functions multiplied by the real combinations of spherical harmonics. The real combinations are listed below:

$$\begin{aligned}
s(\vec{r}) &= \frac{1}{\sqrt{4\pi}} \\
p_x(\vec{r}) &= \sqrt{\frac{3}{4\pi}}\sin\theta\cos\phi = \sqrt{\frac{3}{4\pi}}\frac{x}{r} \\
p_y(\vec{r}) &= \sqrt{\frac{3}{4\pi}}\sin\theta\sin\phi = \sqrt{\frac{3}{4\pi}}\frac{y}{r} \\
p_z(\vec{r}) &= \sqrt{\frac{3}{4\pi}}\cos\theta = \sqrt{\frac{3}{4\pi}}\frac{z}{r} \\
d_{3z^2-r^2}(\vec{r}) &= \sqrt{\frac{5}{16\pi}}\left(3\cos^2\theta - 1\right) = \sqrt{\frac{5}{16\pi}}\frac{1}{r^2}\left(3z^2 - r^2\right) \\
d_{x^2-y^2}(\vec{r}) &= \sqrt{\frac{15}{16\pi}}\sin^2\theta\cos 2\phi = \sqrt{\frac{5}{16\pi}}\frac{1}{r^2}\left(x^2 - y^2\right) \\
d_{xy}(\vec{r}) &= \sqrt{\frac{15}{16\pi}}\sin^2\theta\sin 2\phi = \sqrt{\frac{15}{4\pi}}\frac{1}{r^2}xy \\
d_{yz}(\vec{r}) &= \sqrt{\frac{15}{16\pi}}\sin 2\theta\sin\phi = \sqrt{\frac{15}{4\pi}}\frac{1}{r^2}yz \\
d_{xz}(\vec{r}) &= \sqrt{\frac{15}{16\pi}}\sin 2\theta\cos\phi = \sqrt{\frac{15}{4\pi}}\frac{1}{r^2}xz,
\end{aligned} \tag{66}$$

where in the second part we used the cartesian coordinate transformation

$$\begin{aligned}
x &= r\sin\theta\cos\phi \\
y &= r\sin\theta\sin\phi \\
z &= r\cos\theta.
\end{aligned} \tag{67}$$

We want to move to a new coordinate system, where the first orbital is at the origin, and the second on the z-axis. We do this by linear translation followed by two subsequent rotations.

The first translation is trivial $-\vec{v}_a$, and after this the first orbital is at the origin and the second at position $\vec{v} = \vec{v}_b - \vec{v}_a$ (figure 7b). Here for simplicity I assume that the $\vec{v}$ is in the positive octant.

In this coordinate system we define two angles. The first ϕ_1 is the angle between the basis vector $\hat{e}_2$ and the projection of the vector $\vec{v}$ to the $\hat{e}_1, \hat{e}_2$-plane:

$$\phi_1 = \arcsin\left(\frac{v_1}{\sqrt{v_1^2 + v_2^2}}\right) = \arccos\left(\frac{v_2}{\sqrt{v_1^2 + v_2^2}}\right), \tag{68}$$

where we use the notation $\vec{v} = v_1\hat{e}_1 + v_2\hat{e}_2 + v_3\hat{e}_3$ and $v = |\vec{v}|$. The second angle θ_2 is the angle between the basis vector $\hat{e}_3$ and the vector $\vec{v}$:

$$\theta_2 = \arcsin\left(\frac{\sqrt{v_1^2 + v_2^2}}{v}\right) = \arccos\left(\frac{v_3}{v}\right). \tag{69}$$

The first rotation along the z-axis corresponds to a coordinate transformation

$$\begin{aligned} x &\mapsto \cos\phi_1 \cdot x + \sin\phi_1 \cdot y \\ y &\mapsto -\sin\phi_1 \cdot x + \cos\phi_1 \cdot y \\ z &\mapsto z, \end{aligned} \tag{70}$$

and the second rotation along the x-axis to

$$\begin{aligned} x &\mapsto x \\ y &\mapsto \cos\theta_2 \cdot y + \sin\theta_2 \cdot z \\ z &\mapsto -\sin\theta_2 \cdot y + \cos\theta_2 \cdot z. \end{aligned} \tag{71}$$

Combining the two subsequent rotations gives us the complete transformation rules for the coordinates

$$\begin{aligned} &x \mapsto \cos\phi_1 \cdot x + \sin\phi_1 \cdot y \mapsto \cos\phi_1 \cdot x + \sin\phi_1\cos\theta_2 \cdot y + \sin\phi_1\sin\theta_2 \cdot z \\ &y \mapsto -\sin\phi_1 \cdot x + \cos\phi_1 \cdot y \mapsto -\sin\phi_1 \cdot x + \cos\phi_1\cos\theta_2 \cdot y + \cos\phi_1\sin\theta_2 \cdot z \\ &z \mapsto z \mapsto -\sin\theta_2 \cdot y + \cos\theta_2 \cdot z. \end{aligned} \tag{72}$$

To shorten the equations we switch to a notation $\frac{v_1}{v} = \mathbf{x}$, $\frac{v_2}{v} = \mathbf{y}$, $\frac{v_3}{v} = \mathbf{z}$, $\mathbf{x}^2 + \mathbf{y}^2 = \boldsymbol{\alpha}$ and $\mathbf{x}^2 - \mathbf{y}^2 = \boldsymbol{\beta}$. With this notation the rotation angles are:

$$\sin\phi_1 = \frac{\mathbf{x}}{\sqrt{\boldsymbol{\alpha}}} \qquad \cos\phi_1 = \frac{\mathbf{y}}{\sqrt{\boldsymbol{\alpha}}} \tag{73}$$

$$\sin\theta_2 = \sqrt{\boldsymbol{\alpha}} \qquad \cos\theta_2 = \mathbf{z} \tag{74}$$

and the coordinate transformations

$$\begin{aligned} x &\mapsto \frac{\mathbf{y}}{\sqrt{\boldsymbol{\alpha}}}x + \frac{\mathbf{zx}}{\sqrt{\boldsymbol{\alpha}}}y + \mathbf{x}z \\ y &\mapsto -\frac{\mathbf{x}}{\sqrt{\boldsymbol{\alpha}}}x + \frac{\mathbf{yz}}{\sqrt{\boldsymbol{\alpha}}}y + \mathbf{y}z \\ z &\mapsto -\sqrt{\boldsymbol{\alpha}}y + \mathbf{z}z. \end{aligned} \tag{75}$$

We can find out how the orbitals transform by substituting these into the formula of the orbitals:

$$\begin{aligned} p_x &= \sqrt{\frac{3}{4\pi}}\frac{1}{r}x \mapsto \sqrt{\frac{3}{4\pi}}\frac{1}{r}\left(\frac{\mathbf{y}}{\sqrt{\boldsymbol{\alpha}}}x + \frac{\mathbf{zx}}{\sqrt{\boldsymbol{\alpha}}}y + \mathbf{x}z\right) \\ &= \frac{\mathbf{y}}{\sqrt{\boldsymbol{\alpha}}}p_x + \frac{\mathbf{xz}}{\sqrt{\boldsymbol{\alpha}}}p_y + \mathbf{x}p_z \\ p_y &\mapsto -\frac{\mathbf{x}}{\sqrt{\boldsymbol{\alpha}}}p_x + \frac{\mathbf{yz}}{\sqrt{\boldsymbol{\alpha}}}p_y + \mathbf{y}p_z \\ p_z &\mapsto -\sqrt{\boldsymbol{\alpha}}p_y + \mathbf{z}p_z. \end{aligned} \tag{76}$$

Now we are ready to calculate the integrals between the p-orbitals at arbitrary positions. The overlap integral is over the whole space, so the limits are not affected by the transformations. Many of the integrals are zero by symmetry, the ones that remain are listed in table 3 in ref. 80. I will calculate here the integrals between the p-orbitals.

$$\begin{aligned} &\int_1 p_x(\vec{r}_1 - \vec{v}_a)p_x(\vec{r}_1 - \vec{v}_b) = \int_1 p_x(\vec{r}_1)p_x(\vec{r}_1 - \vec{v}) \\ &= \int_1 \left(\left[\frac{\mathbf{y}}{\sqrt{\boldsymbol{\alpha}}}p_x(\vec{r}_1) + \frac{\mathbf{xz}}{\sqrt{\boldsymbol{\alpha}}}p_y(\vec{r}_1) + \mathbf{x}p_z(\vec{r}_1)\right] \times \right. \\ &\left.\left[\frac{\mathbf{y}}{\sqrt{\boldsymbol{\alpha}}}p_x(\vec{r}_1 - v\hat{z}) + \frac{\mathbf{xz}}{\sqrt{\boldsymbol{\alpha}}}p_y(\vec{r}_1 - v\hat{z}) + \mathbf{x}p_z(\vec{r}_1 - v\hat{z})\right]\right) \\ &= \text{(the cross terms are zero by symmetry)} \\ &= \frac{\mathbf{y}^2}{\boldsymbol{\alpha}}\underbrace{\int_1 p_x(\vec{r}_1)p_x(\vec{r}_1 - v\hat{z})}_{=S_{pp\pi}(v)} + \frac{\mathbf{x}^2\mathbf{z}^2}{\boldsymbol{\alpha}}\underbrace{\int_1 p_y(\vec{r}_1)p_y(\vec{r}_1 - v\hat{z})}_{=S_{pp\pi}(v)} \\ &\quad + \mathbf{x}^2\underbrace{\int_1 p_z(\vec{r}_1)p_z(\vec{r}_1 - v\hat{z})}_{=S_{pp\sigma}(v)} \\ &= \mathbf{x}^2 S_{pp\sigma}(v) + \frac{\mathbf{y}^2 + \mathbf{x}^2\overbrace{\mathbf{z}^2}^{=1-\boldsymbol{\alpha}}}{\boldsymbol{\alpha}}S_{pp\pi}(v) \\ &= \mathbf{x}^2 S_{pp\sigma}(v) + \frac{1}{\boldsymbol{\alpha}}(\overbrace{\mathbf{y}^2 + \mathbf{x}^2}^{=\boldsymbol{\alpha}} - \mathbf{x}^2\boldsymbol{\alpha})S_{pp\pi}(v) \\ &= \mathbf{x}^2 S_{pp\sigma}(v) + \left(1 - \mathbf{x}^2\right)S_{pp\pi}(v). \end{aligned} \tag{77}$$

$$
\begin{aligned}
&\int_1 p_x(\vec{r}_1 - \vec{v}_a) p_y(\vec{r}_1 - \vec{v}_b) = \int_1 p_x(\vec{r}_1) p_y(\vec{r}_1 - \vec{v}) \\
&= \int_1 \left(\left[\frac{\mathbf{y}}{\sqrt{\boldsymbol{\alpha}}} p_x(\vec{r}_1) + \frac{\mathbf{xz}}{\sqrt{\boldsymbol{\alpha}}} p_y(\vec{r}_1) + \mathbf{x} p_z(\vec{r}_1) \right] \times \right. \\
&\quad \left. \left[-\frac{\mathbf{x}}{\sqrt{\boldsymbol{\alpha}}} p_x(\vec{r}_1 - v\hat{z}) + \frac{\mathbf{yz}}{\sqrt{\boldsymbol{\alpha}}} p_y(\vec{r}_1 - v\hat{z}) + \mathbf{y} p_z(\vec{r}_1 - v\hat{z}) \right] \right) \\
&= (\text{the cross terms are zero by symmetry}) \\
&= -\frac{\mathbf{xy}}{\boldsymbol{\alpha}} \int_1 p_x(\vec{r}_1) p_x(\vec{r}_1 - v\hat{z}) \\
&\quad + \frac{\mathbf{xyz}^2}{\boldsymbol{\alpha}} \int_1 p_y(\vec{r}_1) p_y(\vec{r}_1 - v\hat{z}) + \mathbf{xy} \int_1 p_z(\vec{r}_1) p_z(\vec{r}_1 - v\hat{z}) \\
&= -\frac{1}{\boldsymbol{\alpha}} \mathbf{xy} \overbrace{(1 - \mathbf{z}^2)}^{=\boldsymbol{\alpha}} S_{pp\pi}(v) + \mathbf{xy} S_{pp\sigma}(v) \\
&= \mathbf{xy} S_{pp\sigma}(v) - \mathbf{xy} S_{pp\pi}(v).
\end{aligned}
\tag{78}
$$

$$
\begin{aligned}
&\int_1 p_x(\vec{r}_1 - \vec{v}_a) p_z(\vec{r}_1 - \vec{v}_b) = \int_1 p_x(\vec{r}_1) p_y(\vec{r}_1 - \vec{v}) \\
&= \int_1 \left(\left[\frac{\mathbf{y}}{\sqrt{\boldsymbol{\alpha}}} p_x(\vec{r}_1) + \frac{\mathbf{xz}}{\sqrt{\boldsymbol{\alpha}}} p_y(\vec{r}_1) + \mathbf{x} p_z(\vec{r}_1) \right] \times \right. \\
&\quad \left. \left[-\sqrt{\boldsymbol{\alpha}} p_y(\vec{r}_1 - v\hat{z}) + \mathbf{z} p_z(\vec{r}_1 - v\hat{z}) \right] \right) \\
&= (\text{the cross terms are zero by symmetry}) \\
&= -\mathbf{xz} \int_1 p_y(\vec{r}_1) p_y(\vec{r}_1 - v\hat{z}) + \mathbf{xz} \int_1 p_z(\vec{r}_1) p_z(\vec{r}_1 - v\hat{z}) \\
&= \mathbf{xz} S_{pp\sigma}(v) - \mathbf{xz} S_{pp\pi}(v).
\end{aligned}
\tag{79}
$$

To obtain all the coefficients listed in table 4 in ref. [80] we need to first rotate the d-orbitals in the same way as we did for the p-orbitals in equation (76). Then we simply need to evaluate all the non-zero integrals between s, p and d orbitals.